

The Role of Penetrating Gas Streams in Setting the Dynamical State of Galaxy Clusters

E. Zinger^{1*}, A. Dekel¹, Y. Birnboim¹, A. Kravtsov² & D. Nagai³

¹*Center for Astrophysics and Planetary Science, Racah Institute of Physics, The Hebrew University, Jerusalem 91904, Israel*

²*Department of Astronomy & Astrophysics, The University of Chicago, Chicago, IL 60637 USA*

³*Department of Physics, Yale University, New Haven, CT 06520, USA*

Accepted 2016 May 25. Received 2016 May 25; in original form 2015 October 18

ABSTRACT

We utilize cosmological simulations of 16 galaxy clusters at redshifts $z = 0$ and $z = 0.6$ to study the effect of inflowing streams on the properties of the X-ray emitting intra-cluster medium. We find that the mass accretion occurs predominantly along streams that originate from the cosmic web and consist of heated gas. Clusters that are unrelaxed in terms of their X-ray morphology are characterized by higher mass inflow rates and deeper penetration of the streams, typically into the inner third of the virial radius. The penetrating streams generate elevated random motions, bulk flows and cold fronts. The degree of penetration of the streams may change over time such that clusters can switch from being unrelaxed to relaxed over a time-scale of several gigayears.

Key words: galaxies: clusters: general – galaxies: clusters: intracluster medium.

1 INTRODUCTION

The high temperatures achieved by the gas within the potential wells of clusters of galaxies lead to strong X-ray emission, of the order of 10^{43} – 10^{46} erg s^{−1} (Peterson & Fabian 2006). This allows a unique vista into the dynamics of the gas within the dark matter halo, which is unavailable in less massive systems.

Observations reveal that clusters are complex dynamic systems whose inner structure poses challenging open questions. These include the differences in the dynamical state between ‘relaxed’ and ‘unrelaxed’ clusters (Buote & Tsai 1996), the origin of ‘cool-core’ (CC) versus ‘non-cool-core’ (NCC) clusters (Sanderson et al. 2006, 2009a), the bulk motions and cold fronts in the intracluster medium (ICM; Burns 1998), and the wide metal enrichment of the ICM (Mushotzky & Loewenstein 1997; De Grandi et al. 2004). The fact that clusters form at the nodes of the cosmic web and are fed through streams may allow us to make progress in the understanding of these open issues concerning the ICM.

By and large, the ICM gas is assumed to be in hydrostatic equilibrium within the potential well of the dark matter halo, achieving temperatures of $\sim 10^7$ – 10^8 K. Gas accretion into the central regions occurs gradually as the gas loses energy to radiation, primarily in the X-ray (Sarazin

1988). However, detailed observations reveal that in many clusters the X-ray morphology of the cluster points to an unrelaxed (NR) dynamical state, as attested by an abundance of substructure, irregular isophotes and prominent filamentary structures. Clusters in which these features are absent are considered relaxed (R).

It is commonly assumed that the dynamically unrelaxed state is the result of one or many merger events in the cluster. In this paper we propose that the existence of large-scale gas streams which penetrate into the centre of cluster can also play an equally important role in determining whether a cluster is R or NR.

The treatment of clusters up until now has been largely as quasi-spherical systems, but it has now become clear that one must consider the full three dimensional structure of clusters to truly understand these systems. A key to a better understanding of the dynamics of clusters is taking into account the fact that clusters form at the nodes of the cosmic web.

The simplified model of spherical accretion has in recent years been replaced by a more realistic picture where the accretion on to and through dark matter haloes is predominantly along streams that follow the large-scale filaments of the cosmic web. Typically, a few, nearly co-planar streams feed each halo (Danovich et al. 2012). The massive haloes of rich clusters represent high-sigma peaks in the density fluctuation field, namely they are much more massive than the Press–Schechter mass of typical haloes at that time.

* E-mail: elad.zinger@mail.huji.ac.il

At high redshift, as these haloes were fed by streams that were narrower than the virial radius of the halo and denser than the mean virial density. Due to the high density, the radiative cooling time of the gas in these streams was shorter than the local compression time, preventing the formation of a stable virial shock within the streams, while such a shock is present in the rest of the halo virial surface (Birnbom & Dekel 2003; Dekel & Birnbom 2006). This allowed the streams in massive haloes at high redshift to penetrate through the virial radius into the inner halo (Kereš et al. 2005; Ocirk et al. 2008; Dekel et al. 2009; Kereš et al. 2009). As we shall see, the streams can still be found in massive clusters at $z = 0$ albeit with very different thermodynamic properties.

These penetrating streams are likely to affect the inner ICM. As we will show, the dichotomy between R and NR clusters is strongly related to the presence of deeply penetrating streams in the cluster. The penetrating streams can carry large quantities of gravitational energy into the cluster centre which drive random gas motions and result in an unrelaxed state. Clusters in which streams do not penetrate into the centre are found to be dynamically relaxed.

Observational studies of clusters have detected filamentary structures which may be the streams we find in the simulations. Observations of the Coma cluster (e.g., Finoguenov et al. 2003; Brown & Rudnick 2011; Bonafede et al. 2013; Simionescu et al. 2013) reveal diffuse X-ray emissions from filamentary structures which extend out to the cluster outskirts. Eckert et al. 2015 report the detection of filamentary structures of hot gas extending over 8 Mpc in the cluster Abell 2744. The filaments of the cosmic web from which the gas streams originate have also been detected as extended X-ray sources between clusters (Werner et al. 2008; Dietrich et al. 2012).

The dynamical state of the cluster has been found to correlate strongly with the presence, or absence, of a CC in the cluster. Clusters which are dynamically relaxed typically host a CC while NR clusters are typically classified as NCC (Smith et al. 2005; Sanderson et al. 2009b; Chen et al. 2007). The common wisdom is that a CC cannot easily form in a dynamically disturbed environment. It is important to note that while the simulations analysed here result in both R and NR clusters the simulations do *not* reproduce the CC versus NCC bimodality.

The penetrating streams in NR clusters may also impact the metal enrichment of the ICM. There are observational indications of high metal enrichment throughout the ICM, even at large distances from the BCG (Rebusco et al. 2006; Simionescu et al. 2015). This suggests that the ICM gas is churned and mixed, thereby scattering the metals throughout the cluster. Turbulent motions created by the inflow of gas, smoothly and through mergers, may act as an efficient mixing process.

Gas motions in the ICM are observed to be highly complex. Markevitch et al. (2000) and Churazov et al. (2003) find evidence of inner shocks and ‘cold fronts’ which are associated with bulk motions of gas within the ICM (see Markevitch & Vikhlinin 2007 for a review). Cold fronts are contact discontinuities between gas of different temperatures and densities which maintain pressure equilibrium along the discontinuity, as opposed to shocks in which the pressure jumps in value across the shock front. These cold fronts

Cluster	M_{vir} ($10^{14} M_{\odot}$)	R_{vir} (Mpc)	T_{vir} (10^7 K)	V_{vir} (km s^{-1})	State R/NR
CL101	22.1	3.37	10.1	1678	NR
CL102	13.7	2.88	7.4	1433	NR
CL103	15.7	3.01	8.1	1497	NR
CL104	11.9	2.74	6.7	1365	R
CL105	12.0	2.75	6.7	1369	NR
CL106	9.5	2.54	5.8	1266	NR
CL107	6.6	2.26	4.5	1125	NR
CL3	6.3	2.22	4.4	1107	R
CL5	3.1	1.76	2.8	875	R
CL6	3.3	1.80	2.9	894	NR
CL7	3.3	1.78	2.8	886	R
CL9	1.9	1.48	1.7	739	NR
CL10	1.3	1.32	1.6	658	R
CL11	1.8	1.45	1.9	721	NR
CL14	1.7	1.43	1.8	709	R
CL24	0.86	1.14	1.2	569	NR

Table 1. Cluster properties at $z = 0$. State refers to R versus NR systems. Virial quantities were calculated for an overdensity of $\Delta_{\text{vir}} = 337$ above the mean density of the universe.

Cluster	M_{vir} ($10^{14} M_{\odot}$)	R_{vir} (Mpc)	T_{vir} (10^7 K)	V_{vir} (km s^{-1})	State R/NR
CL101	3.3	1.29	4.0	1053	R
CL102	3.3	1.28	4.0	1051	NR
CL103	2.9	1.23	3.7	1009	NR
CL104	7.2	1.66	6.7	1362	R
CL105	6.2	1.58	6.0	1296	NR
CL106	2.6	1.18	3.3	965	NR
CL107	2.9	1.22	3.6	1002	NR
CL3	2.8	1.21	3.6	995	NR
CL5	1.8	1.04	2.6	858	NR
CL6	2.4	1.15	3.2	946	NR
CL7	2.3	1.13	3.1	929	R
CL9	1.2	0.91	2.0	744	NR
CL10	1.1	0.89	1.9	730	R
CL11	0.86	0.78	1.5	643	NR
CL14	0.99	0.86	1.8	703	NR
CL24	0.37	0.62	0.9	505	NR

Table 2. Cluster properties at $z = 0.6$. State refers to R versus NR systems. Virial quantities were calculated for an overdensity of $\Delta_{\text{vir}} = 224$ above the mean density of the universe.

are found to form as a result of motions of bodies of gas within the ICM (Ascasibar & Markevitch 2006; Roediger et al. 2011). As we will see, deeply penetrating streams in NR clusters can generate cold fronts in the cluster centre.

The paper is organized as follows: in §2, we describe our suite of simulated systems. In §3, we compare between the R and NR clusters in the simulation suite and analyse the source of differences between them. In §4, the mass accretion along inflowing gas streams is presented and a link between stream penetration and relaxedness is established. §5 examines the respective roles of gas streams and merging substructure in determining the dynamical state of the cluster. In §6, we discuss our results and in §7 summarize our main findings.

2 SIMULATIONS

The simulation suite analysed in this study is comprised of 16 cluster-sized systems at $z = 0$ spanning a mass range of $8.6 \times 10^{13} - 2.2 \times 10^{15} M_{\odot}$, and their most massive progenitors at $z = 0.6$.

The systems were extracted from cosmological simulations in a flat Λ cold dark matter (Λ CDM) model: $\Omega_m = 1 - \Omega_{\Lambda} = 0.3$, $\Omega_b = 0.04286$, $h = 0.7$, and $\sigma_8 = 0.9$, where Ω_m and Ω_{Λ} are the density parameters of mass and cosmological constant, the Hubble constant is $100h \text{ km s}^{-1} \text{ Mpc}^{-1}$, and σ_8 is the power spectrum normalization on an $8h^{-1} \text{ Mpc}$ scale at $z = 0$. The simulations were carried out with the Adaptive Refinement Tree (ART) N -body +gas-dynamics AMR code (Kravtsov 1999), an Eulerian code that uses adaptive refinement in space and time, and (non-adaptive) refinement in mass (Klypin et al. 2001) to reach the high dynamic range required to resolve cores of haloes formed in self-consistent cosmological simulations.

The computational boxes of the large-scale cosmological simulations were either $120h^{-1} \text{ Mpc}$ or $80h^{-1} \text{ Mpc}$, and the simulation grid was adaptively refined to achieve a peak spatial resolution of ~ 7 and $5h^{-1} \text{ kpc}$, respectively. These simulations are discussed in detail in Kravtsov et al. (2006), Nagai et al. (2007a) and Nagai et al. (2007b).

Besides the basic dynamical processes of collision-less matter (dark matter and stars) and gas-dynamics, several physical processes critical for galaxy formation are incorporated: star formation, metal enrichment and feedback due to Type II and Type Ia supernovae and self-consistent advection of metals. The cooling and heating rates of the gas take into account Compton heating and cooling of plasma, heating by the UV background (Haardt & Madau 1996), and atomic and molecular cooling, which is tabulated for the temperature range $10^2 \text{ K} < T < 10^9 \text{ K}$, a grid of metallicities, and UV intensities using the CLOUDY code (version 96b4; Ferland et al. 1998). The CLOUDY cooling and heating rates take into account metallicity of the gas, which is calculated self-consistently in the simulation, so that the local cooling rates depend on the local metallicity of the gas. The star formation recipe incorporated in these simulations is observationally motivated (e.g. Kennicutt 1998) and the code also accounts for the stellar feedback on the surrounding gas, including injection of energy and heavy elements (metals) via stellar winds, supernovae, and secular mass loss.

In this paper, the virial quantities of mass, radius, velocity and temperature (M_{vir} , R_{vir} , V_{vir} , T_{vir}) of the clusters are defined for an overdensity $\Delta_{\text{vir}} = 337$ at $z = 0$ and $\Delta_{\text{vir}} = 224$ at $z = 0.6$ above ρ_{mean} , the mean mass density of the universe (Bryan & Norman 1998). The properties of the clusters for $z = 0$ and $z = 0.6$ are summarized in Tables 1 and 2, respectively.

The virial quantities are customarily set based on the spherical ‘top-hat’ model which follows the expansion and subsequent collapse of an initial uniform density perturbation in an Einstein–de Sitter universe. Virialization of the halo in the model occurs when the radius of the halo is one half of its radius at maximum expansion, and the resulting mean density in the halo is found to be 178 times the mean density of the universe. Extending this model for a Λ CDM universe results in a higher value of $\Delta_{\text{vir}} \simeq 337$ (Bryan & Norman 1998).

The virial parameters M_{vir} and R_{vir} are therefore defined to be

$$\frac{3M_{\text{vir}}}{4\pi R_{\text{vir}}^3} = \Delta_i \rho_{\text{ref}}, \quad (1)$$

with various choices in the literature for the overdensity parameter ($\Delta_i = 178, 200, 337$) and reference density ρ_{ref} – either ρ_{crit} or $\rho_{\text{mean}} = \rho_{\text{crit}} \Omega_m$. Additional distance scales for clusters are sometimes set by overdensity factors of 500 and 1500.¹

The simulations do not include an AGN feedback mechanism, and this may lead to unrealistic conditions in the central region of the cluster. The AGN feedback may provide the heating source to avert the cooling flow problem in cluster cores. In this paper we do not address the issue of the cooling flow problem but rather focus on the division into R and NR clusters. Excluding AGN feedback allows us to separate the role of gas streams in determining the conditions in the inner regions of the ICM from that of the AGN.

Since the simulations do not include the relevant cluster core physics, such as heating by AGN and thermal conduction, the CC versus NCC dichotomy cannot be properly recreated in our cluster suite. Recent studies by Rasia et al. 2015 and Hahn et al. 2015 have shown that the dichotomy can be recreated in simulations if the proper numerical models are implemented.

As a result of these shortcomings, the entire suite of simulated clusters suffers from overcooling in the central core ($\lesssim 0.01R_{\text{vir}}$), which leads to a nonphysical high density cusp. However, the simulations do capture the dynamics and structure at larger scales, recreating the R versus NR dichotomy. Specifically, the radial range of $0.05 - 0.25R_{\text{vir}}$, in which we study the effects of stream penetration, is well resolved and can give a reliable picture of the large-scale effects which determine the relaxedness of clusters.

Traditionally, R_{vir} is used to demark the edge of a halo (Molnar et al. 2009). However, this definition has been shown to be inadequate for clusters since other important measures such as the ‘splashback’ radius (Diemer & Kravtsov 2014; More et al. 2015) and the virial accretion shock have been shown to extend to well beyond the virial radius (Lau et al. 2015). In this work we consider the regions between R_{vir} and the virial shock front as part of the cluster, and for the study at hand, we shall define the virial accretion shock as the edge of the cluster. An in-depth analysis of the definition of the edge of a cluster, specifically in the context of quenching of star formation in satellite galaxies, appears in a separate paper (Zinger et al., in preparation).

The classification of the simulated clusters R or NR (see Tables 1 and 2) was carried out to emulate as close as possible the methods employed by observational studies. The classification is described in detail in Nagai et al.

¹ The dependence of the scaling parameters on the choice of Δ and reference density can be found for a given choice of halo model. As an example, for an isothermal sphere density profile, different choices of Δ and ρ_{ref} will result in different values of M_{vir} and R_{vir} such that

$$\frac{M_{\text{vir},1}}{M_{\text{vir},2}} \propto \frac{R_{\text{vir},1}}{R_{\text{vir},2}} \propto \left(\frac{\Delta_1 \rho_{\text{ref},1}}{\Delta_2 \rho_{\text{ref},2}} \right)^{-1/2}, \quad (2)$$

and thus $R_{200} \simeq 1.3R_{337}$.

(2007a,b), and is based on mock *Chandra* X-ray images of the clusters which were created on a scale of $R_{500,c}$ (an overdensity of $\Delta_c = 500$ above the critical density ρ_{crit}) where $R_{500,c} \simeq 0.45 R_{\text{vir}}$ (eq. 2). Based on the mock observations, clusters are identified as R if they possess regular X-ray morphology with no secondary luminosity peaks and minimal deviations from elliptical symmetry. By contrast, NR clusters are those with distinct secondary luminosity peaks, filamentary X-ray structures, or significant shifts of the centres of isophotes. This classification was carried out for each cluster in three orthogonal Cartesian projections, and only clusters which appear relaxed in all three projections are classified as R. Conversely, clusters which appear unrelaxed in at least one projection are classified as NR (see also Lau et al. 2011). We revisit the issue of this classification in relation to the gas streams in §5

Since we will be dealing with gas motions and inflowing streams, it is only proper that we elucidate how the centre of the cluster and the inertial frame of reference used to measure the gas velocities are defined. The cluster centre is defined by the location of the dark matter particle with the highest local matter density (Lau et al. 2009). To define the inertial frame, a centre-of-mass velocity profile was calculated for the three velocity components for each cluster in the suite. A radius was selected where the profiles were seen to level off (typically at $\sim 1\text{--}2R_{\text{vir}}$). The gas velocities are then measured with respect to the centre-of-mass velocity as calculated for the gas within that radial limit. Since the profiles are relatively flat and constant over a wide range of radii, the centre-of-mass velocity is largely insensitive to the choice of the radial limit.

3 PROPERTIES OF R VERSUS NR CLUSTERS

We examine the differences between the R and NR populations of clusters in our simulation suite and attempt to link the dynamical state of the clusters to the intensity and penetration of the gas streams.

3.1 Hydrodynamic Stability

We begin with an examination of the hydrodynamical stability of the ICM to gravitational collapse. To this end, we probe the dynamics of the gas when smoothed over an intermediate scale, i.e. one that is larger than the cell-size yet smaller than the relevant cluster scales of several 100 kpc.

To do so we make use of a generalized Jeans equation for the radial velocity component adapted for use in an Eulerian system (rather than a system of particles), averaged over spherical shells (Rasia et al. 2004 and see also Lau et al. 2013 for a similar derivation)

$$\begin{aligned} \bar{\rho} \frac{\partial \bar{v}_r}{\partial t} + \bar{\rho} \bar{v}_r \frac{\partial \bar{v}_r}{\partial r} = \\ - \bar{\rho} \frac{\partial \bar{\Phi}}{\partial r} - \frac{\partial}{\partial r} \left(\frac{k_B}{m} \bar{\rho} T \right) - \frac{\partial}{\partial r} \left(\bar{\rho} \sigma_{rr}^2 \right) \\ - \frac{\bar{\rho}}{r} \left(2\sigma_{rr}^2 - \sigma_{\theta\theta}^2 - \sigma_{\varphi\varphi}^2 \right) + \frac{\bar{\rho}}{r} \left(\bar{v}_\theta^2 + \bar{v}_\varphi^2 \right). \quad (3) \end{aligned}$$

Like the Jeans equation, this equation is derived as the first moment of the Boltzmann equation for the distribution function averaged over velocity space and over a spherical shell

of a given radius. The result is a motion equation for a spherical shell, in which all the values represent averages of the form:

$$\bar{\rho}(r) = \frac{1}{4\pi} \int f(\vec{x}, \vec{v}) d\Omega d^3v \quad (4)$$

$$\bar{v}_\alpha(r) = \frac{1}{4\pi\bar{\rho}} \int v_\alpha f(\vec{x}, \vec{v}) d\Omega d^3v, \quad (5)$$

where $f(\vec{x}, \vec{v})$ is the distribution function in phase space and σ_{ij}^2 is defined as

$$\sigma_{ij}^2(r) = \overline{v_i v_j} - \bar{v}_i \bar{v}_j. \quad (6)$$

Since we wish to apply the equation to an Eulerian hydro-simulation, in which gas motions are smoothed on the scale of the cell size, we assume that the σ^2 terms can be separated into a contribution from the microscopic velocities, which are isotropic and represented by the temperature T , and the macroscopic cell velocities, which are used to determine the terms in eq. (6). We therefore add a thermal pressure term (second term on the RHS of eq. (3)) to account for the contribution of the subgrid velocities. The thermal pressure is derived for an Ideal Gas equation of state, $\bar{\rho} k_B T m^{-1}$, where k_B is the Boltzmann constant and m is the average particle mass. The temperature T in this term is the mass-weighted mean temperature of the spherical shell.

There has been some contention as to the validity of using the Jeans equation, which describes collisional dynamics, for the treatment of the collisional gas in simulations. Suto et al. (2013) have argued this point and suggested that the Euler equation is a more appropriate choice. However, Lau et al. (2013) have shown that one can obtain the generalized Jeans equation *with* the added thermal term by a spatial averaging of the Euler equation, and that both methods are valid, and in fact, equivalent.

The LHS of eq. (3) is simply the full convective derivative of the shell velocity. The terms on the RHS are the force terms, the first relating to the gravitational attraction, the second is force due to thermal pressure and the third is the force related to ‘pressure’ from macroscopic motions of the gas (‘turbulence’). The other terms are related to anisotropy and asphericity and vanish for a spherically symmetric ($v_\theta = v_\varphi = 0$) and isotropic ($\sigma_{rr}^2 = \sigma_{\theta\theta}^2 = \sigma_{\varphi\varphi}^2$) systems. The final three terms, the force due to random gas motions, anisotropy and asphericity, comprise the non-thermal contribution to the hydrodynamical stability of the system.

For the case of a system in steady state ($\partial v_r / \partial t = 0$) and equilibrium ($v_r = 0$), the LHS of eq. (3) is zero and the equation takes the form

$$\begin{aligned} - \bar{\rho} \frac{\partial \bar{\Phi}}{\partial r} - \frac{\partial}{\partial r} \left(\frac{k_B}{m} \bar{\rho} T \right) - \frac{\partial}{\partial r} \left(\bar{\rho} \sigma_{rr}^2 \right) \\ - \frac{\bar{\rho}}{r} \left(2\sigma_{rr}^2 - \sigma_{\theta\theta}^2 - \sigma_{\varphi\varphi}^2 \right) + \frac{\bar{\rho}}{r} \left(\bar{v}_\theta^2 + \bar{v}_\varphi^2 \right) = 0. \quad (7) \end{aligned}$$

Employing this equation allows us to examine whether a system is indeed in steady state equilibrium and, more importantly, what is the relative contributions of the thermal and non-thermal parts to balancing the force of gravity. We recast eq. (7) by dividing it by the amplitude of the gravitational force

$$\frac{F_T + F_{NT}}{|F_G|} = 1, \quad (8)$$

where

$$F_G = -\frac{\partial \Phi}{\partial r} = -\frac{GM(<r)}{r^2} \quad (9)$$

$$F_T = -\frac{\partial}{\partial r} \left(\frac{k_B}{m} \bar{\rho} T \right) \quad (10)$$

$$F_{NT} = -\frac{\partial}{\partial r} \left(\bar{\rho} \overline{\sigma_{rr}^2} \right) - \frac{\bar{\rho}}{r} \left(2\overline{\sigma_{rr}^2} - \overline{\sigma_{\theta\theta}^2} - \overline{\sigma_{\varphi\varphi}^2} \right) + \frac{\bar{\rho}}{r} \left(\overline{v_\theta^2} + \overline{v_\varphi^2} \right). \quad (11)$$

In Figs. 1a and 1b, we show the terms of eq. (8) averaged separately over the R and NR clusters respectively, at $z = 0$. The same is shown for $z = 0.6$ in Figs. 1c and 1d. A striking difference between the two populations is that for R clusters, the thermal and non-thermal terms balance the gravitational force within R_{vir} , indicating that these clusters are indeed in a steady state equilibrium. The same cannot be said of the NR clusters, where the total contributions are greater than the gravitational pull. This implies that the full derivative of the radial velocity (LHS of eq. 3) is positive, which can describe either a cluster which is expanding ($v_r > 0$) or one which is collapsing ($v_r < 0$) but whose internal pressure (thermal and non-thermal) is in the process of balancing the collapse (Nelson et al. 2014a). An examination of the mass-accretion rate in these clusters (Figs. 3b and 3d) shows that the mass is inflowing into the clusters, thus we are observing clusters in which the pressure is building up to balance the collapse. In this way we see that the NR nature of the clusters, originally defined by observational measures, is manifest in the dynamical properties of the cluster as well.

In both populations, the thermal component accounts for ~ 90 per cent of the support against gravity, but in NR clusters the non-thermal component is ~ 20 per cent of the gravitational force, roughly twice as much as in R clusters. It is this excess which embodies the ‘unrelaxedness’ of the clusters. In the outskirts of both the R and NR clusters, beyond R_{vir} , the thermal pressure steadily drops leaving the gas unsupported against the pull of gravity in these regions.

Another difference between the two populations is seen in the central regions of the clusters, within $0.2R_{\text{vir}}$. In this region in the R clusters, the contribution of the thermal pressure is seen to gradually decline corresponding to a rise in the non-thermal contributions (see also Lau et al. 2009; Molnar et al. 2010; Vazza et al. 2011; Nelson et al. 2014b). The NR clusters, on the other hand, show no such change. To understand this issue, we must ascertain which of the non-thermal terms is responsible for this increase, which is at odds with observational limits on the non-thermal support (Sanders et al. 2011; Pinto et al. 2015).

We decompose the non-thermal support into the ‘turbulent’ pressure and the anisotropic and aspherical components, as detailed in eq. (11), and average the profiles separately over R and NR clusters. This decomposition is shown in Fig. 2 for the clusters at $z = 0$ and $z = 0.6$.

The rise in non-thermal support in the very central regions of R clusters ($\lesssim 0.1R_{\text{vir}}$), is due to the anisotropic component, and to a lesser degree the aspherical component, both of which are due to tangential motions, which both rise gradually towards the centre. The source for this rise is a strong, ordered rotational motion in the centres of these clusters, as was shown in Lau et al. 2011. The build-up of the rotational motion is due to the overcooling in the

centre of the cluster, and is therefore an unphysical feature of the simulation we do not expect to find in cluster observations.

The dominant non-thermal component in clusters is the pressure due to random motions, which accounts for ~ 50 per cent of the gravitational support outside R_{vir} , and drops to ~ 20 per cent within R_{vir} for NR clusters and only several per cent in R clusters. The asphericity in all clusters can be seen to be small at all radii. In the outskirts ($\gtrsim R_{\text{vir}}$) there is a significant amount of anisotropy which dwindles to several per cent at $r \approx 0.5R_{\text{vir}}$.

In the NR population, there is a clear difference between the two epochs, with the anisotropic and aspherical component playing a minor role in the central regions at $z = 0$ in contrast to their very significant contribution in the central parts at $z = 0.6$.

3.2 Mass Inflow into the Cluster

We compare the R and NR cluster populations in terms of the gas accreted on to the systems, by studying the mass inflow rate through radial shells,

$$\dot{M}(r) = \iint_{\Omega} \rho [(\vec{v} - \vec{v}_{\text{cm}}) \cdot \hat{r}] r^2 d\Omega, \quad (12)$$

where ρ and \vec{v} are the density and velocity of a gas element and \vec{v}_{cm} is the centre of mass velocity of the system, defined on a scale of $\sim R_{\text{vir}}$ (see §2). In practice, the density and velocity data grids in the simulations were sampled on a spherical shell of a given radius, while maintaining a constant surface area for each sampling point. The sampling points were distributed along 256 latitudinal rings, 256 points uniformly distributed along each ring, with the spacing between the rings adjusted according to the distance between points along the rings to ensure a constant surface area per sampling point. Thus, the rings in the ‘equatorial’ regions are more densely packed than in close to the ‘poles’.

We separate the inflowing ($v_r < 0$) and outflowing ($v_r > 0$) material for each cluster and average the mass inflow/outflow rate over the R and NR clusters separately. In Fig. 3, we show the inflow and outflow rates for the clusters at $z = 0$ and $z = 0.6$, respectively.

In the outer regions of the cluster, out to the virial shock front which extends out to $\sim 2R_{\text{vir}}$ (Lau et al. 2015, Zinger et al., in preparation), the inflow rate is roughly equal to analytic estimates for the average inflow rate at R_{vir} based on the EPS formalism (Birnbom et al. 2007):

$$\frac{\dot{M}}{M} \simeq 0.1 M_{15}^{0.15} a^{-2.25} \text{Gyr}^{-1}, \quad (13)$$

where $M_{15} \equiv M_{\text{vir}}/10^{15} M_{\odot}$ and $a = (1+z)^{-1}$ is the expansion parameter of the universe². This estimate is expected to be largely independent of radius, is identical for both the dark matter and baryons (Dekel et al. 2013), and is found to be consistent with cosmological simulations (Wechsler et al. 2002; Neistein & Dekel 2008).

² The power 2.25, which is chosen to fit the results from EPS and simulations at $z < 1$, is a deviation from 5/2, the value that can be simply derived analytically for the EdS regime at $z > 1$ (Dekel et al. 2013). The power 0.15 is determined by the slope of the power spectrum.

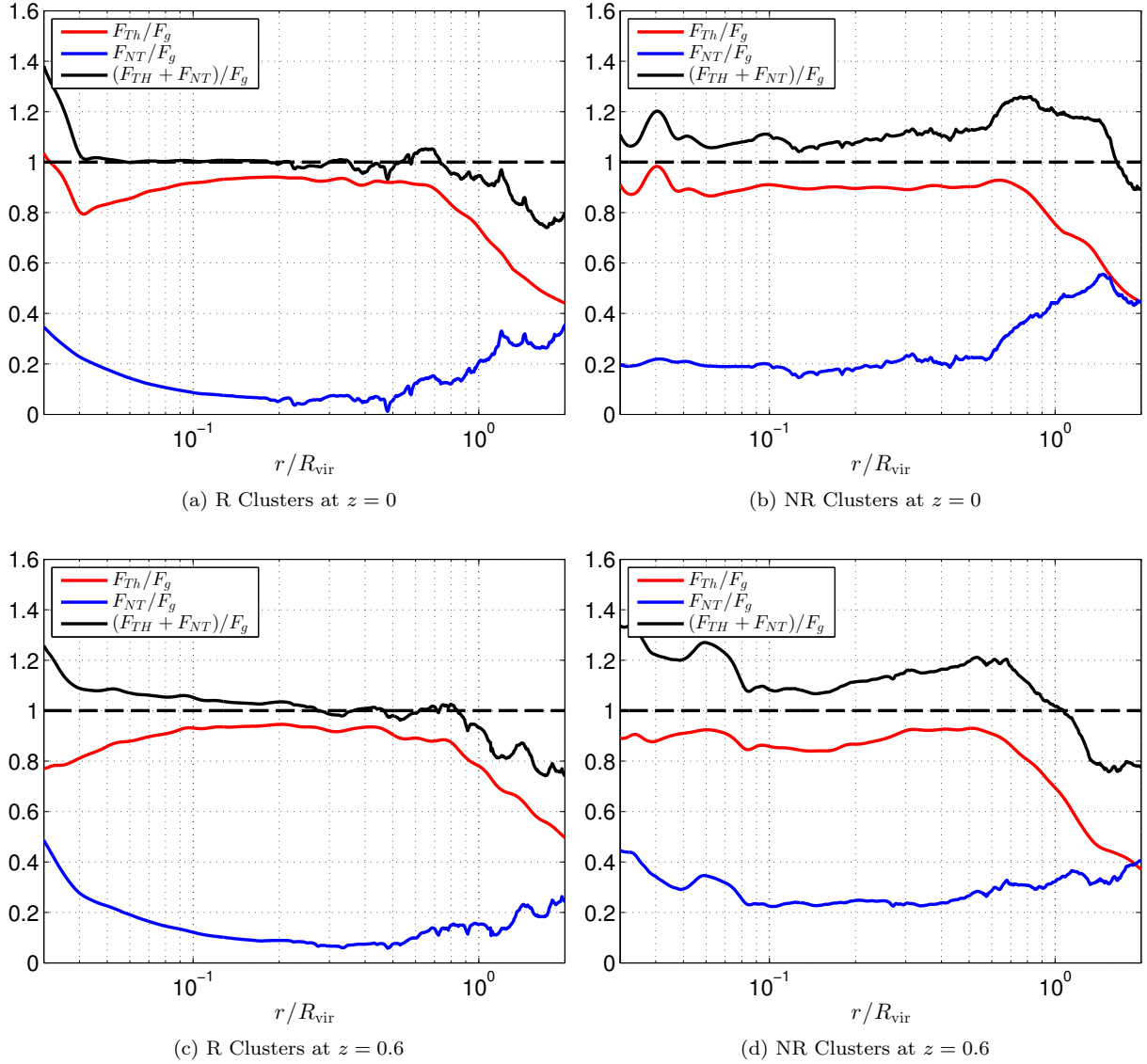


Figure 1. The hydrodynamic stability of the clusters at $z = 0$ (top) and $z = 0.6$ (bottom) is explored via a generalized form of the Jeans equation eq. (8) for spherical shells. The ratio of the thermal to gravitational force (red) is shown alongside the non-thermal to gravitational force ratio (blue). The sum of the two ratios is shown in black, and a value of 1 corresponds to a balance between the gravity and the thermal and non-thermal pressure support, in a steady-state cluster. The profiles are averaged over the R clusters (a) & (c) and NR clusters (b) & (d) separately. Gravity is balanced by the pressure in the R clusters but in the NR population, due to the higher contribution of non-thermal pressure, the systems are unbalanced and cannot be said to be in steady state.

The differences between the R and NR population are striking – in both epochs the inflow and outflow rates in the NR systems are larger by roughly a factor of 2 at all radii. More mass is being driven into the NR clusters, and the gravitational energy released as a result of the inflow into the potential well (see §4.2) leads to the build-up of random motions, as seen in Figs. 3b and 3d.

An interesting feature seen in Fig. 3 is the very tight scatter in the inner parts of R clusters, compared with the much larger scatter in the NR population. The main reason for this feature is the similarity of the inflow and outflow profiles of the different R clusters, and in particular the dearth of substructure in these systems compared to the NR pop-

ulation. We discuss the role of substructure and mergers in determining the relaxedness of a cluster in §5.

4 GAS STREAMS

In the previous section a link was established between the relaxedness of a cluster and the mass inflow rate into the cluster. We now turn to examine in detail the way gas accretes on to a cluster and specifically the filamentary nature of the accretion, along gas streams, and examine the effect they may have on the ICM, especially in the central regions.

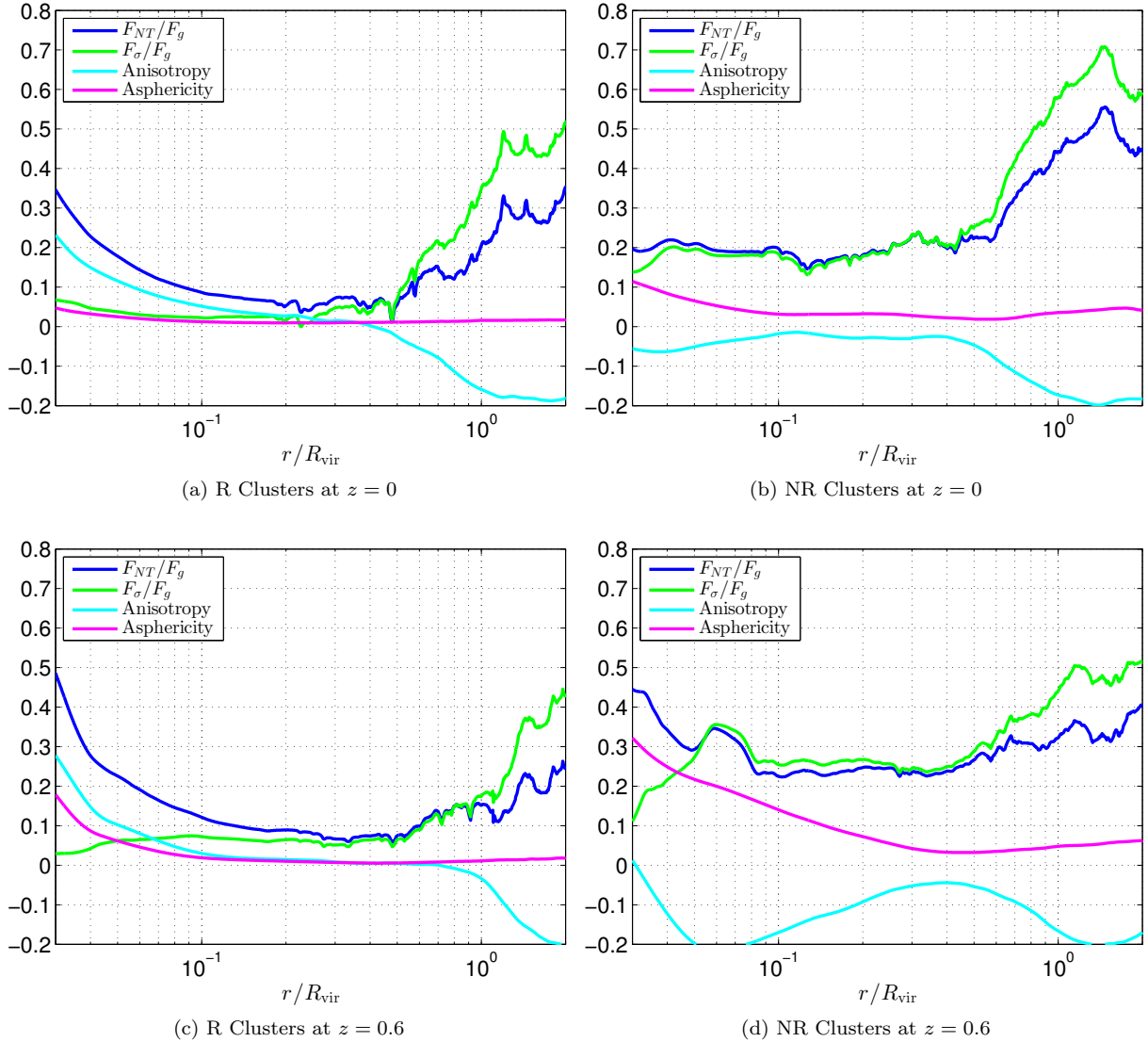


Figure 2. Analysing the non-thermal pressure support in the clusters at $z = 0$ (top) and $z = 0.6$ (bottom). Following eq. (11), the non-thermal part of the generalized Jeans equation (blue) is decomposed into a ‘turbulent’ pressure term (green) an anisotropic term (cyan) and an asphericity term (magenta). The decomposition is averaged over the R clusters (a) & (c) and NR clusters (b) & (d) separately. The pressure due to random motions is the dominant component except in the very central areas in the R clusters, where an ordered rotational motion is responsible for the increase in the contribution of the asphericity and anisotropic terms. In the NR clusters the terms relating to anisotropy and asphericity are more important, especially at $z = 0.6$.

4.1 Properties of Gas Streams

In Fig. 4, we show the temperature, density, entropy and mass inflow rate of the gas in the form of colour-maps for a thin equatorial slice in the cluster CL6, focusing on the regions where the streams enter the system beyond R_{vir} . It is clear that the mass inflow, even in the central parts, is dominated by gas streams which flow into the cluster and extend well beyond R_{vir} (see also Figs. 7 and 8). The accretion of baryonic mass into haloes is known to occur predominately along the dark matter filaments of the cosmic web (Klar & Mücke 2012; Gheller et al. 2015), both in the form of clumpy accretion (Vazza et al. 2013) and also, as smooth streams, as can be seen in these simulations.

The streams are best seen in terms of mass inflow rate

and entropy since the gas flow is mostly adiabatic along the stream and the entropy is conserved, even as the stream is compressed by the ambient gas and its temperature and density increase as a result. In the outer regions beyond R_{vir} , their temperature is also lower, enhancing the entropy contrast with their surroundings.

However, this gas inflow cannot be termed a ‘cold flow’ since the temperature within the streams is lower only by a factor of a few than the surrounding medium. This is due to the gas being heated first when crossing the cylindrical shock surrounding the filaments, and subsequently by shock-heating within the supersonic streams as they flow into the system. As a result, the gas temperature in a stream is already well above 10^6 K when it enters the system (Werner et al. 2008). At these temperatures, radiative cooling oc-

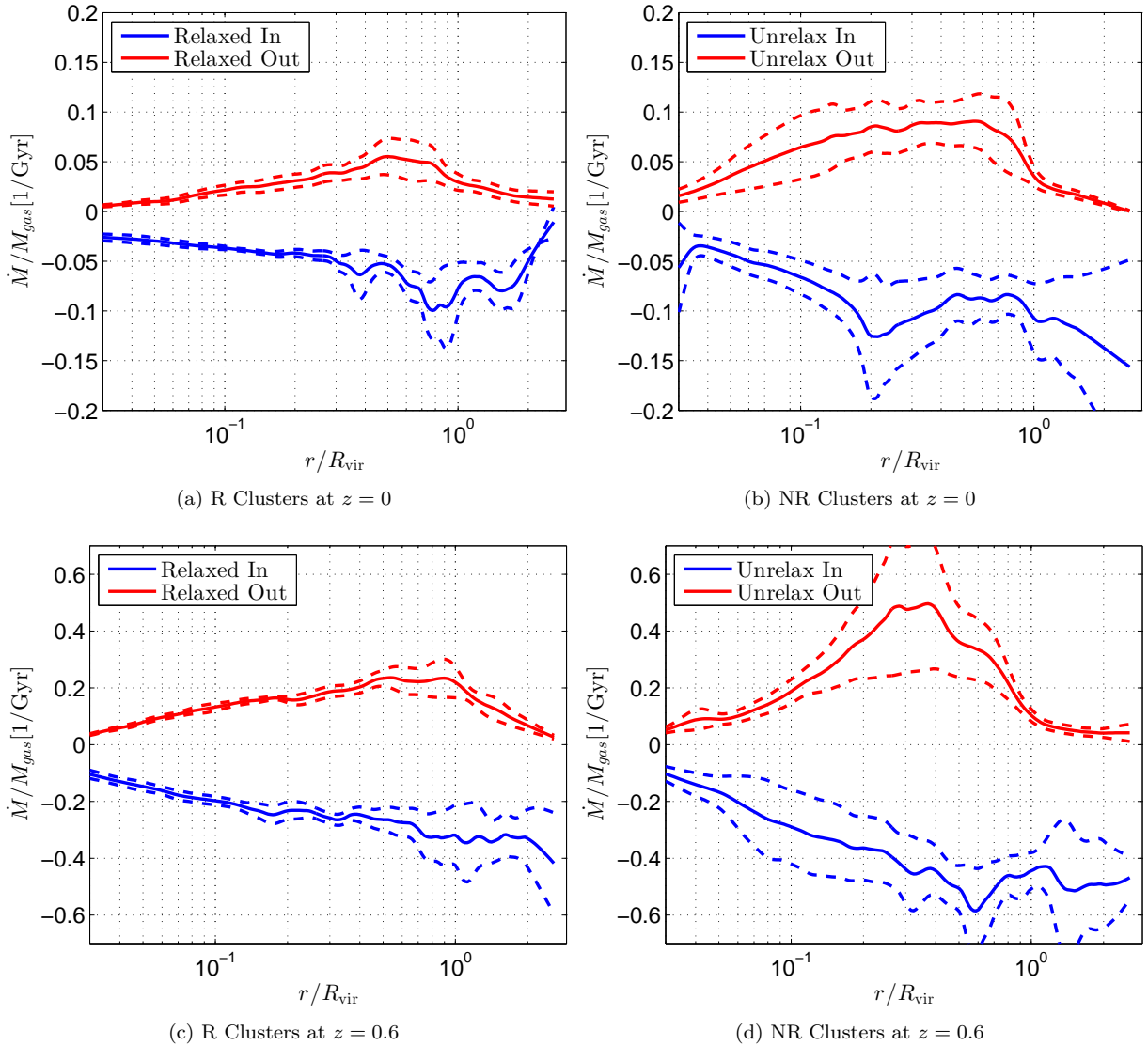


Figure 3. The mean mass inflow and outflow rates averaged over the population of R clusters (a) & (c) and NR clusters (b) & (d) at $z = 0$ (top) and $z = 0.6$ (bottom). The mean inflow rate is shown in solid blue and the mean outflow rate in red. Dashed lines mark a 1σ deviation about the mean. NR clusters are characterized by higher inflow rates at all radii, as well as higher outflows.

curs predominately through Bremsstrahlung radiation which scales as $\propto T^{1/2}$. A drop in temperature in a radiatively cooling parcel of gas will lead to a drop in the cooling efficiency, and thus runaway cooling cannot develop (as it does for lower temperatures) and the gas will remain hot. The heating of the gas, by compression and by shocks, in the stream continues as the supersonic stream flows into the cluster, especially within R_{vir} as the density of the ICM increases.

Unlike the ‘cold flows’ seen in simulations of high redshift galaxies (Birnboim & Dekel 2003; Kereš et al. 2005; Dekel & Birnboim 2006; Dekel et al. 2009; Kereš et al. 2009), these gas streams feeding the clusters are more aptly described by the term ‘warm streams’, due to the pre-heating in the filaments. After crossing R_{vir} , the streams are heated to $T_{\text{vir}} \gtrsim 10^7$ K by the time they reach the inner regions ($r \lesssim 0.25R_{\text{vir}}$).

In Fig. 5, we examine the streams in the cluster CL6 both at the scale of R_{vir} (Figs. 5a and 5b) and zooming in

on the central regions (Figs. 5c and 5d). The mass inflow rate is shown, which allows easy identification of the streams. In addition, we show the Mach number of the gas flows with respect to the surrounding hot medium. The Mach number \mathcal{M} shown is the ratio between the local gas velocity and the typical speed of sound at a given radius

$$c_s(r) = \sqrt{\left. \frac{\partial P}{\partial \rho} \right|_s} = \sqrt{\gamma \frac{k_B \bar{T}}{\mu m_p}}, \quad (14)$$

where the second expression derives from the ideal gas equation of state used to describe the gas. The factor γ is the adiabatic index ($\gamma = 5/3$ for a monoatomic gas), k_B is the Boltzmann constant, $\mu m_p \simeq 0.59m_p$ is the average particle mass (m_p being the proton mass), and \bar{T} is the mass-weighted mean temperature of a spherical shell (including the stream) at a given radius.

A very prominent supersonic ($\mathcal{M} > 1$) stream coming

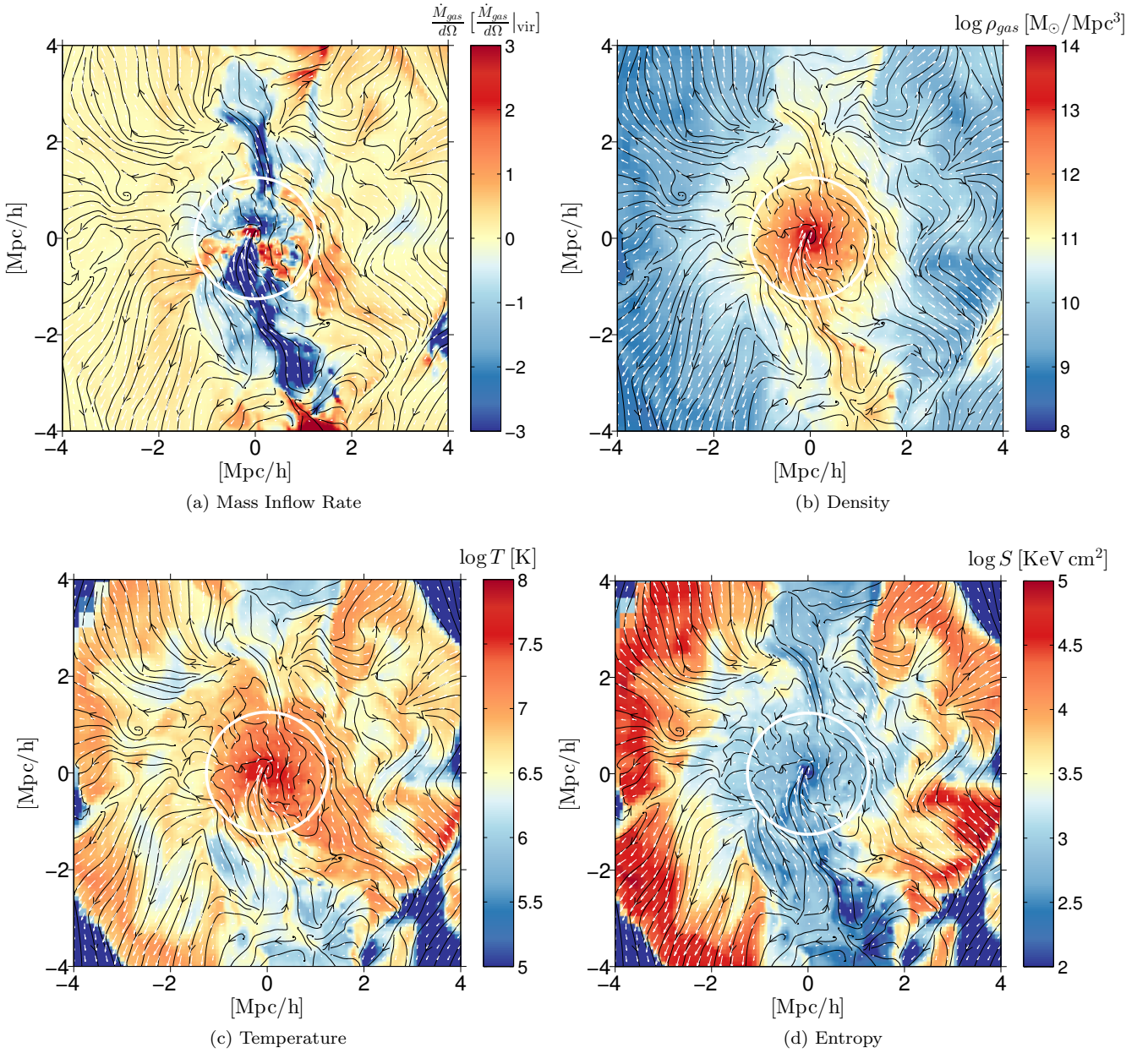


Figure 4. Maps of mass inflow rate (a), density (b), temperature (c) and entropy (d) in an equatorial slice of $180h^{-1}$ kpc of the cluster CL6 at $z = 0$, focusing on the areas between R_{vir} and the accretion shock. The velocity field in the plane is described by white arrows and in addition, by black streamlines. The virial radius is marked by a white circle. It is clear that mass inflow rate occurs almost exclusively along the streams puncturing the hot medium which are clearly seen in the entropy map. The streams are only marginally cooler than the hot medium at large radii and are heated to T_{vir} within R_{vir} .

from outside R_{vir} can be identified at the bottom of the picture and flowing into the central region. Focusing on the centre of the cluster, we see the stream overshooting the centre (leading to an abrupt change in sign of the radial inflow rate, from blue to red). The stream collides with gas flowing in the opposite direction leading to the formation of a shock front, as can be seen in the temperature and pressure maps of the region (Figs. 6a and 6b, respectively). The shock front, marked by the red arrow in Fig. 6, is arc-shaped and characterized by a sharp change in the pressure and density. Shocks such as these, generated by the gas streams, are the mech-

anism for transforming the gravitational energy brought in by the gas streams into heat and random motions.

Just below the shock, a contact discontinuity, also known as a ‘Cold Front’, can be seen as a sharp change in the temperature map, marked by a blue arrow (see also Nagai & Kravtsov 2003). The contact discontinuity is in pressure equilibrium and thus is not noticeable in the pressure map. An in-depth analysis of this shock and ‘cold front’ is presented in a future paper (Zinger et al., in preparation).

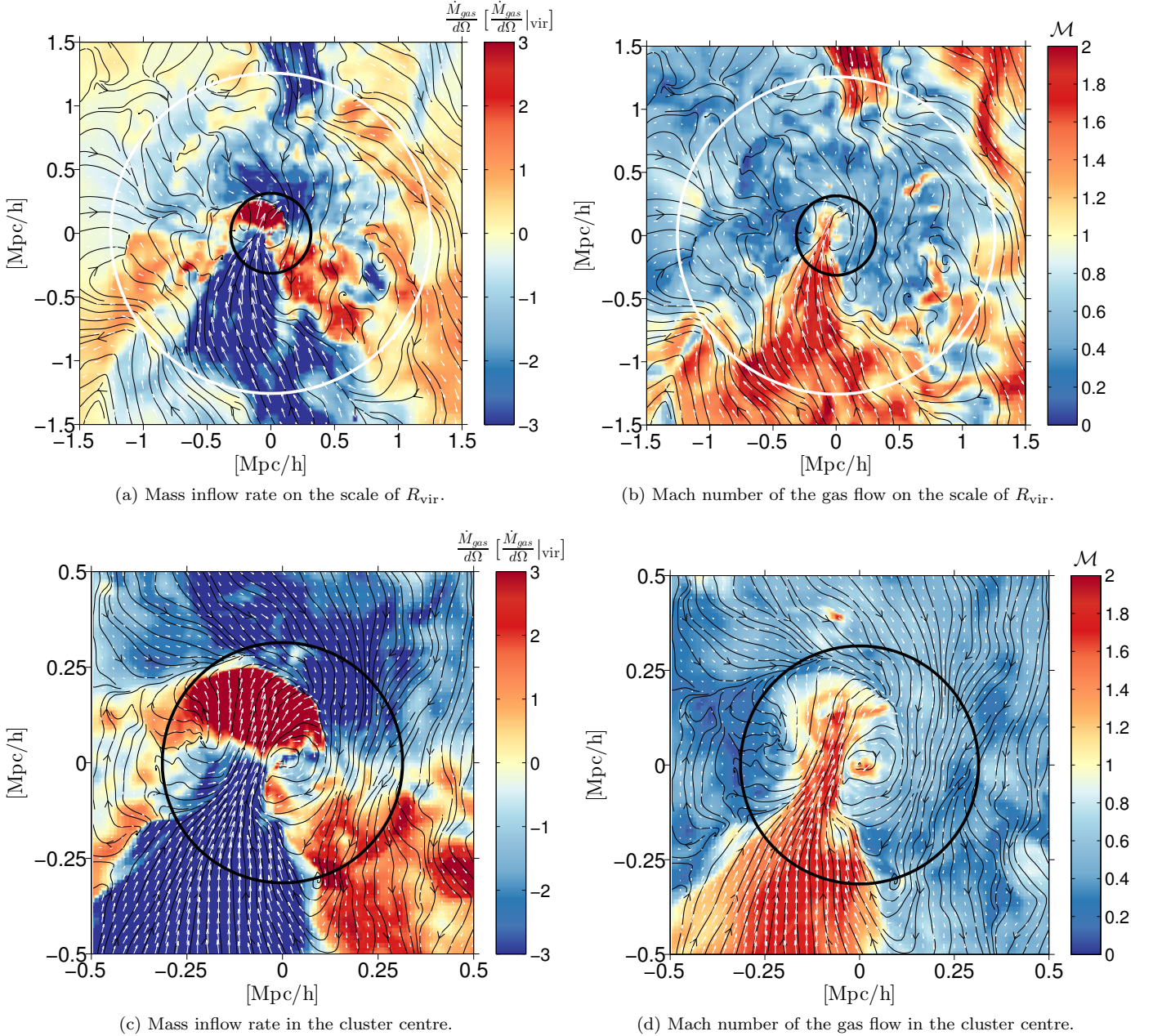


Figure 5. Maps of mass inflow rate (left) and Mach number (right) in a thin equatorial slice of the NR cluster CL6, also shown in Fig. 4, at $z = 0$ shown on the scale of R_{vir} (a) & (b) and focusing on the central regions (c) & (d). R_{vir} is marked by a white circle and a $0.25R_{\text{vir}}$ radius black circles marks the inner regions. The Mach number \mathcal{M} is the ratio of the local velocity and the sonic speed derived from the shell averaged temperature. A supersonic ($\mathcal{M} > 1$) stream enters from the bottom and penetrates to the very centre of the cluster. The abrupt change in the sign of the inflow rate in the up-wards flowing stream (transition from blue to red) is due to the stream overshooting the centre of the system. A shock front forms where the stream collides with the medium.

4.2 Energy Deposition by the Gas Streams

A deeply penetrating stream, like the stream discussed above, can funnel energy into the centre of the cluster. As we will see, the streams typically flow towards the centre till they are stopped and the ordered flow is dispersed into random motions (e.g., Figs. 5 and 7 to 9). We can estimate the energy deposition rate associated with a stream by following it from outside the system $r_{\text{out}} \sim 2R_{\text{vir}}$ until it dissipates at an inner radius r_{in} .

The energy accretion rate is

$$\dot{E}_{\text{str}} = \dot{E}_{\text{gain}} - \dot{E}_{\text{cool}} = \dot{E}_{\text{grav}} + \dot{E}_{\text{kin}} + \dot{E}_{\text{int}} - \dot{E}_{\text{cool}}, \quad (15)$$

where the first three terms in the second equality account for the gravitational, kinetic and internal (thermal) energy brought in by the stream, and the fourth term accounts for the energy lost to radiation along the flow. The energy deposited in the inner regions of the ICM will heat the gas or increase the random motions until it is eventually radiated away.

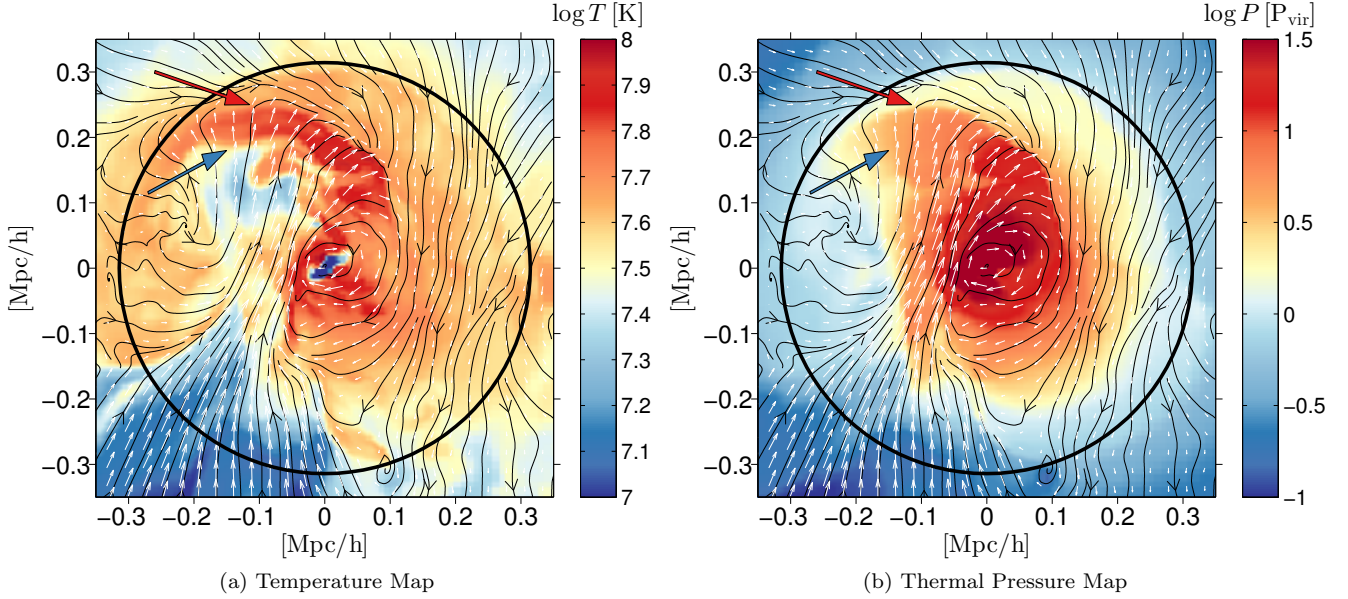


Figure 6. Zoom in on the central region of the cluster CL6 previously shown in Figs. 4 and 5, in temperature (a) and pressure (b). A shock is clearly evident where the upward flowing stream collides with gas flowing from the top of the picture, marked by a red arrow. Just below the shock, a contact discontinuity (‘cold front’) can be seen, marked by a blue arrow.

The gain in gravitational potential energy due to the inflow along the potential gradient, given the mass accretion rate in a stream \dot{M}_{str} , can be expressed as

$$\dot{E}_{\text{grav}} \approx |\Delta\Phi(r_{\text{in}}, r_{\text{out}})|\dot{M}_{\text{str}}, \quad (16)$$

where the potential gain in a spherically symmetric halo, travelling from r_2 to an inner radius r_1 ($r_2 > r_1$), can be expressed as $|\Delta\Phi| = \phi V_{\text{vir}}^2$ with

$$\phi(r_1, r_2) = -\frac{V^2(r_2)}{V_{\text{vir}}^2} + \frac{V^2(r_1)}{V_{\text{vir}}^2} + \int_{r_1/R_{\text{vir}}}^{r_2/R_{\text{vir}}} \frac{3\rho(r')}{\rho_v} r' dr', \quad (17)$$

where $V^2(r) = GM(r)r^{-1}$ and

$$\rho_v = \frac{3M_{\text{vir}}}{4\pi R_{\text{vir}}^3} = \Delta_{\text{vir}}\rho_{\text{mean}}, \quad (18)$$

which follows from eq. (1) (Dekel & Birnboim 2008). The gain in gravitational energy eq. (16) is therefore

$$\dot{E}_{\text{grav}} \approx \phi V_{\text{vir}}^2 \dot{M}_{\text{str}}. \quad (19)$$

For an NFW density profile (Navarro et al. 1996, 1997) we have

$$\phi(r_1, r_2) = \frac{\ln(1 + c_{\text{vir}}x_1)/x_1 - \ln(1 + c_{\text{vir}}x_2)/x_2}{\ln(1 + c_{\text{vir}}) - c_{\text{vir}}/(1 + c_{\text{vir}})}, \quad (20)$$

where $x_i \equiv r_i/R_{\text{vir}}$ and c_{vir} is the concentration parameter of the halo. For cluster-sized systems c_{vir} is on average (Bullock et al. 2001)

$$c_{\text{vir}} \simeq 4.5M_{15}^{-0.15}a. \quad (21)$$

For a singular isothermal sphere halo density profile we have $\phi(r_1, r_2) = \ln(r_2/r_1)$.

The potential energy gain of a gas parcel infalling from $r_{\text{out}} = R_{\text{vir}}, 2R_{\text{vir}} \& 3R_{\text{vir}}$ to a penetration depth of $r_{\text{in}} = 0.1R_{\text{vir}}$ is $\phi_{\text{NFW}} \approx 2.3, 2.9, 3.2$, respectively. For a penetration depth of $r = 0.5R_{\text{vir}}$ we have $\phi_{\text{NFW}} \approx 0.7, 1.4, 1.7$.

For the typical values quoted above ϕ_{NFW} and ϕ_{Iso} differ by less than 10 per cent.

At the inner radius r_{in} the stream disperses into random motions. Shocks, such as the one seen in detail in Fig. 6 (and several other examples in Fig. 13) are a channel in which the energy in the stream is shared with the ICM. The energy carried by the stream is subsequently dissipated, mostly into thermal energy, within this radius. The time-scale of energy dissipation is set by the largest eddy turnover time both for supersonic and subsonic random motions (Mac Low et al. 1998). The turnover time is set by $t_L \sim L/v_L$ where $L \sim r_{\text{in}}$ is the size of the largest eddy (see Fig. 7b) and $v_L \sim 500 \text{ km s}^{-1}$ is the typical gas velocity. For penetration depths of $r_{\text{in}} 0.25R_{\text{vir}}$ the eddy turnover time is typically $t_L \lesssim 1 \text{ Gyr}$ and for $r_{\text{in}} 0.1R_{\text{vir}}$ it is $t_L \lesssim 0.3 \text{ Gyr}$, both of which are shorter than the cluster crossing time which is of the order of several giga years, thus it is reasonable to assume the stream energy is deposited within the central region.

Since we assume the stream is dispersed at the inner radius r_{in} , its velocity is zero at that point and the kinetic energy gain equal to the energy brought in by the stream at the outset

$$\dot{E}_{\text{kin}} = \frac{1}{2}v_{\text{out}}^2\dot{M}_{\text{str}} = \frac{1}{2}\alpha V_{\text{vir}}^2\dot{M}_{\text{str}}, \quad (22)$$

where we have defined $v_{\text{out}} = \sqrt{\alpha}V_{\text{vir}}$ with $\alpha \simeq 1$, since the velocity in the outer regions is of order the virial velocity V_{vir} .

The internal energy per unit mass of the gas in the stream is

$$e_{\text{int}}(T) = \frac{k_B T}{\mu m_p}. \quad (23)$$

Since the stream has ceased to exist at r_{in} its final internal energy is zero, and once again the internal energy contri-

bution is equal to the internal energy of the stream at the outset

$$\dot{E}_{\text{int}} = \frac{k_B T_{\text{out}}}{\mu m_p} \dot{M}_{\text{str}}. \quad (24)$$

The temperature in the outer regions is lower than the virial temperature by a factor of a few at most and we therefore set $T_{\text{out}} = \beta T_{\text{vir}}$ with $\beta \simeq 0.5$. The gain in internal energy is therefore

$$\dot{E}_{\text{int}} = \beta \frac{k_B T_{\text{vir}}}{\mu m_p} \dot{M}_{\text{str}} = \frac{\beta}{2} V_{\text{vir}}^2 \dot{M}_{\text{str}}. \quad (25)$$

The kinetic and internal energy terms specified above represent the total amount of kinetic and thermal energy available at the outset. Obviously, not all of this energy is deposited in the inner radius since some of it will be lost to the ambient medium. These energy losses will eventually be radiated away and we therefore account for them in the energy loss term \dot{E}_{cool} . As we shall shortly show, the total energy loss of the stream to radiation is very small compared to the energy gain.

The gain in energy, neglecting the cooling for now, is

$$\dot{E}_{\text{gain}} = \dot{E}_{\text{grav}} + \dot{E}_{\text{kin}} + \dot{E}_{\text{int}} = (2\phi + \alpha + \beta) \frac{1}{2} \dot{M}_{\text{str}} V_{\text{vir}}^2, \quad (26)$$

where we have used eqs. (19), (22) and (25). The virial velocity for clusters can be expressed as

$$V_{\text{vir}} \simeq \begin{cases} 1290 M_{15}^{1/3} \text{ km s}^{-1} & z = 0 \\ 1520 M_{15}^{1/3} \text{ km s}^{-1} & z = 0.6 \end{cases}. \quad (27)$$

As we saw in §3.2, the total gas inflow rate at R_{vir} is roughly equal to the analytic estimates of Birnboim et al. (2007), eq. (13)

$$\dot{M}_g \simeq 1.5 \times 10^{13} \left(\frac{f_b}{0.14} \right) M_{15}^{1.15} a^{-2.25} \text{ M}_{\odot} \text{ Gyr}^{-1}, \quad (28)$$

where f_b is the universal baryon fraction. A stream which carries a fraction f_s of the baryonic inflow will contribute $\dot{M}_{\text{str}} = f_s \dot{M}_g$.

Thus the power injected by a stream at a dissipation radius of r_{in} is

$$\dot{E}_{\text{gain}} \simeq 8.2 \times 10^{45} f_s (2\phi(r_{\text{in}}, r_{\text{out}}) + \alpha + \beta) \times \left(\frac{f_b}{0.14} \right) M_{15}^{1.82} a^{-2.25} \text{ erg s}^{-1}. \quad (29)$$

For a $10^{15} \text{ M}_{\odot}$ cluster at $z = 0$, assuming typical values of f_b , $\alpha = 1$ and $\beta = 0.5$, the energy injection by a deeply penetrating stream infalling from $2R_{\text{vir}}$ to $0.1R_{\text{vir}}$ is

$$\dot{E}_{\text{gain}} \simeq \begin{cases} 6 \times 10^{46} f_s \text{ erg s}^{-1} & r_{\text{in}} = 0.1 R_{\text{vir}} \\ 3.5 \times 10^{46} f_s \text{ erg s}^{-1} & r_{\text{in}} = 0.5 R_{\text{vir}} \end{cases}. \quad (30)$$

For a $10^{14} \text{ M}_{\odot}$ cluster with the same choice of parameters, the energy injection rate is

$$\dot{E}_{\text{str}} \simeq \begin{cases} 9 \times 10^{44} f_s \text{ erg s}^{-1} & r_{\text{in}} = 0.1 R_{\text{vir}} \\ 5.2 \times 10^{44} f_s \text{ erg s}^{-1} & r_{\text{in}} = 0.5 R_{\text{vir}} \end{cases}. \quad (31)$$

The energy carried in by the streams is sufficiently large to have a noticeable effect on the inner regions of the cluster. However, it is not immediately clear how much of the energy is indeed deposited at the site where the stream dissipates. The potential energy of the gas stream is converted to other

forms of energy by several channels. Some of the energy is radiated away, some is channeled to heating the gas and some is converted to kinetic energy (e.g. turbulence) as the gas velocity increases.

Examining the temperature in the stream we find that it increases by a factor of ~ 10 between R_{vir} and the inner regions, due to the gain in gravitational energy (Fig. 4c). In our analysis, we find that the velocity and velocity dispersion do not increase by more than a factor of a few. In any case, the changes in internal or kinetic energy of the stream do not change the amount of energy in the stream itself (only its form) and thus can still be shared with the ambient gas at the site of stream dissipation. The only energy which is truly removed from the stream is that which is radiated away.

We will now assess the energy losses in the stream and show that they are negligible compared with the energy gain. We may convince ourselves that only a small fraction of the stream energy is lost to radiative cooling along its way by finding an upper limit on the energy lost to cooling, namely the *total* amount of radiative cooling *outside* the inner regions of the cluster $r \gtrsim 0.25 R_{\text{vir}}$.

The radiative cooling rate per unit mass is

$$q = \left(\frac{\chi}{\mu m_p} \right)^2 \rho_g \Lambda(T, Z), \quad (32)$$

where $\chi \simeq 0.52$, μm_p is the average particle mass, ρ_g is the gas density and $\Lambda(T, Z)$ is the atomic radiative cooling function (Sutherland & Dopita 1993), which depends on the gas temperature T and metallicity Z . For a spherically symmetric gas distribution, the total cooling rate in the region between r_{in} and r_{out} is

$$\dot{E}_{\text{cool}} = 4\pi \int_{r_{\text{in}}}^{r_{\text{out}}} q(r') \rho_g(r')^2 r'^2 dr'. \quad (33)$$

Due to the strong density dependence, most of the energy will be radiated from the centre of the cluster. We assume the temperature and metallicity are constant throughout the halo, and scale the gas density profile

$$\hat{\rho}_g(r) \equiv \frac{\rho_g(r)}{f_b \rho_v}, \quad (34)$$

where f_b is the gas fraction in the cluster and ρ_v is defined in eq. (18). The cooling rate is now

$$\dot{E}_{\text{cool}} \simeq 3 \times 10^{44} \Lambda_{-23} M_{15}^2 f_{0.14}^2 \mathcal{I}(r_1/R_{\text{vir}}, r_2/R_{\text{vir}}) \text{ erg s}^{-1}, \quad (35)$$

where $\Lambda_{-23} \equiv \Lambda/10^{-23} \text{ erg cm}^3 \text{ s}^{-1}$, $f_{0.14} \equiv f_b/0.14$ and

$$\mathcal{I}(x_1, x_2) = \int_{x_1}^{x_2} \hat{\rho}_g(y)^2 y^2 dy. \quad (36)$$

For typical density profiles the integral converges quickly for $x_2 \rightarrow \infty$; thus, an upper limit can be defined as $\mathcal{I}_{\text{max}}(x) = \mathcal{I}(x, \infty)$. For cooling beyond the central regions ($r \gtrsim 0.25 R_{\text{vir}}$) both the NFW and isothermal profile result in $\mathcal{I}_{\text{max}}(0.25) \simeq 0.45$.

For relevant temperatures of $T > 10^6 \text{ K}$ one can use the approximation of Dekel & Birnboim (2006) for the cooling function

$$\Lambda_{-23} \simeq 6 Z_{0.3}^{0.7} T_6^{-1} + 0.2 T_6^{1/2}, \quad (37)$$

where $T_6 \equiv 10^6 \text{ K}$ and $Z_{0.3} \equiv (Z/0.3) Z_{\odot}$. For typical values

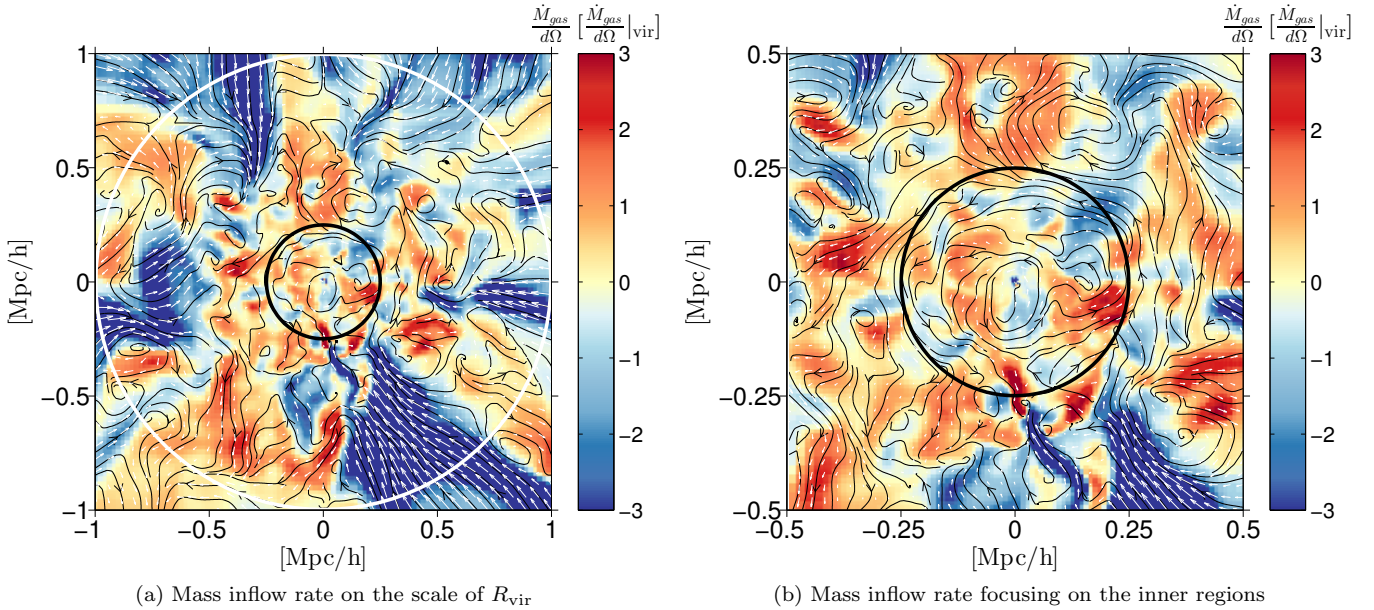


Figure 7. Maps of mass inflow rate in a thin equatorial slice of the R cluster CL14 at $z = 0$, shown on the scale of R_{vir} (a) and focusing on the inner regions (b). White arrows describe the velocity field in addition to black streamlines. The virial radius is marked by a white circle and the black circle demarks the $0.25R_{\text{vir}}$ radius. Several streams can be identified entering the system, e.g. bottom-right and top-left corners in (a), but they stop at $r \approx 0.5R_{\text{vir}}$ and do not penetrate into the central regions in which no coherent flows can be found.

of the mean metallicity, $Z_{0.3} \lesssim 1$ (Tozzi et al. 2003), and virial temperatures in clusters ($10 < T_6 < 100$), we find $\Lambda_{-23} \lesssim 2$. We can therefore set $\mathcal{I}_{\text{max}} = 0.5$ and $\Lambda_{-23} = 2$ to get a strong upper limit on the total cooling rate from the entire cluster volume in the shell $0.25R_{\text{vir}} < r < 2R_{\text{vir}}$,

$$\dot{E}_{\text{cool}} \simeq 3 \times 10^{44} M_{15} f_{0.14}^2 \text{ erg s}^{-1}. \quad (38)$$

This implies that the cooling rate in the streams account for only a small fraction of this energy output. Comparing this to the energy brought in by the streams (e.g. eq. 30), we see that radiative cooling in the streams outside $0.25R_{\text{vir}}$ can remove only a very small fraction of the total energy. We may therefore safely assume that $\dot{E}_{\text{str}} \approx \dot{E}_{\text{gain}}$, and that the expression eq. (29) and estimated values of eqs. (30) and (31) represent the energy deposition of the streams.

We find that the energy associated with an inflowing stream, even one which only accounts for $\lesssim 10$ per cent of the total gas accretion, is in the same range as the typical X-ray luminosity of the cluster which is in the range of 10^{43} – 10^{46} erg s $^{-1}$ (Peterson & Fabian 2006).

Most of the energy carried in by the streams is thus transferred into random motions. The random motions dissipate into heat, but may also drive the sustained growth of magnetic fields (Iapichino & Brüggen 2012) and the subsequent acceleration of Cosmic Rays (CR). The combined contribution of turbulent motions, magnetic fields and CR's to pressure support in the central regions of clusters is of the order of 10 per cent of the thermal pressure support (Churazov et al. 2008), so it is safe to assume that the majority of the energy brought in by the stream is dissipated into heat and eventually radiated away.

The dissipation of random motions is due to the action of viscosity. While it is true that the viscosity may be affected by the presence of magnetic fields and CR's, this will

only change the viscous scale where the dissipation takes place but not the rate of dissipation which is set by the largest eddy turnover time.

As shown above, the largest eddy turnover time is of the order of 0.1–1 Gyr in the central regions of the clusters and thus the energy dissipation should occur over several turnover times, on a time-scale of a few giga years. This value is very similar to those found in observation by Hallman & Jeltama (2011) and Rossetti et al. (2011).

Though we have shown that the streams may carry a substantial amount of energy into the central regions of the cluster in NR clusters, the current simulations, even those classified as NR still suffer from an overcooling problem in the very centre of simulated clusters. Though this may be the result of the numerical limitations of the simulations, it may indicate that the gas streams on their own cannot offset the cooling and that additional physical processes, e.g. AGN feedback and thermal conduction, are still necessary to overcome the cooling-flow problem perhaps even in NR clusters (Rasia et al. 2015).

4.3 Stream Penetration

As we have shown, the gas streams in the NR cluster CL6 penetrate into the very centre of the cluster (Figs. 4 and 5). The penetrating streams carry with them a considerable amount of energy (§4.2) which can be deposited into the central regions. However, examination of other clusters in the simulation suite shows that not all clusters possess deeply penetrating gas streams.

In Figs. 7a and 7b, we examine the cluster CL14 at $z = 0$, on the scale of R_{vir} and focusing on the inner regions. Here too, several gas streams can be identified entering the

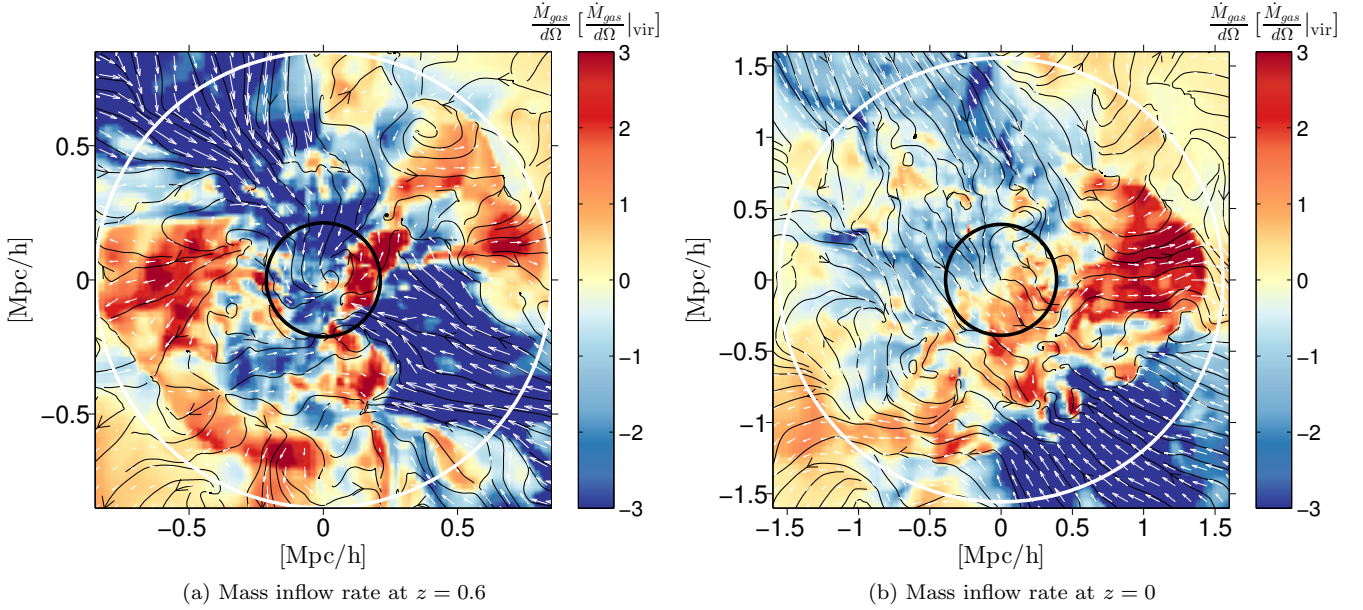


Figure 8. Maps of mass inflow rate in a thin equatorial slice of the cluster CL3 shown at $z = 0.6$ (a) and at $z = 0$ (b). White arrows describe the velocity field in addition to black streamlines. The virial radius is marked by a white circle and the black circle demarks the $0.25R_{\text{vir}}$ radius. At the earlier redshift the streams penetrate to the central regions while at $z = 0$ the streams are stopped at $r \approx 0.5R_{\text{vir}}$.

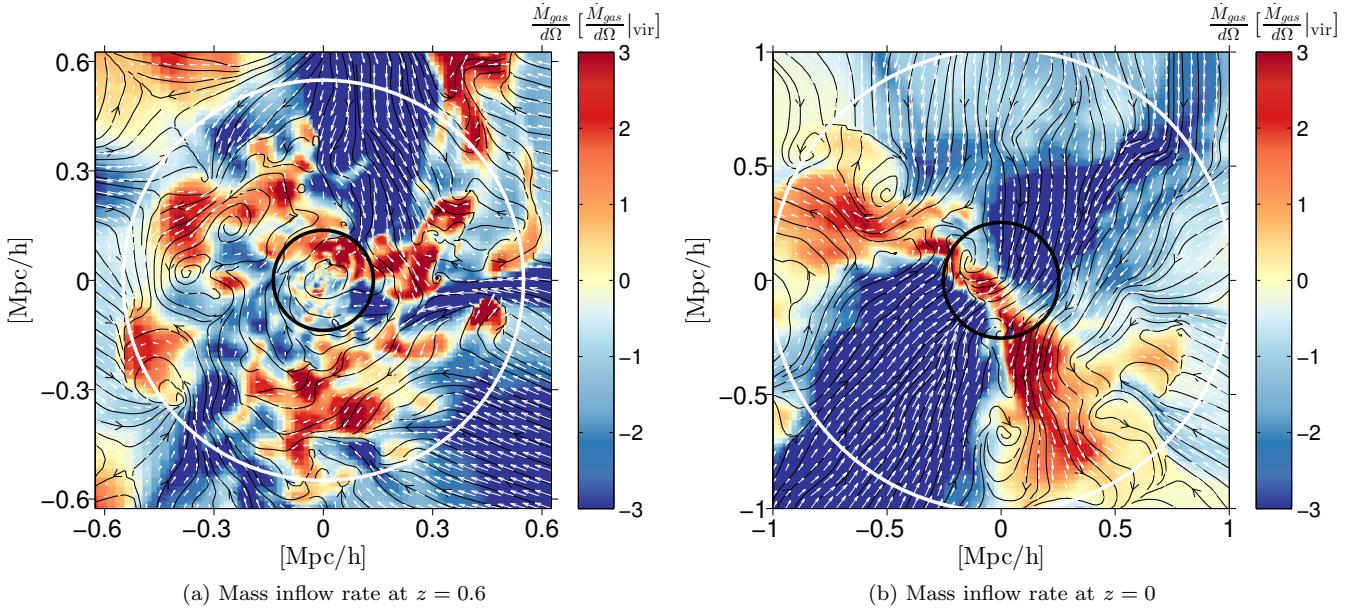


Figure 9. Maps of mass inflow rate in a thin equatorial slice of the cluster CL11 shown at $z = 0.6$ (a) and at $z = 0$ (b). At the earlier redshift, the streams do not penetrate to the central regions while at $z = 0$ the central regions are dominated by deeply penetrating streams.

system, most notably from the top-left and bottom-right corners in Fig. 7a, but all of them stop abruptly at approximately $0.5R_{\text{vir}}$. Examination of the central region shows that no coherent flows are found there, and there is no significant source of mass inflow. Accordingly, the cluster is classified as R.

Comparing the clusters with their progenitors at earlier times shows that the degree of stream penetration into the central areas can change over time. In Fig. 8a, we examine

the cluster CL3 at $z = 0.6$, roughly 5.7 Gyr ago, where the cluster crossing time is 2 Gyr at $z = 0$ and 1.2 Gyr at $z = 0.6$. Two prominent streams enter the system, one from the top-left corner and the other from the bottom-right, and flow unabated into the very centre of the system. Examining the same cluster at $z = 0$ in Fig. 8b shows that the stream from the bottom-right corner now stops at about $0.5R_{\text{vir}}$, whereas the mass flow in the stream from the top-left has dwindled considerably and barely enters the virial radius. The change

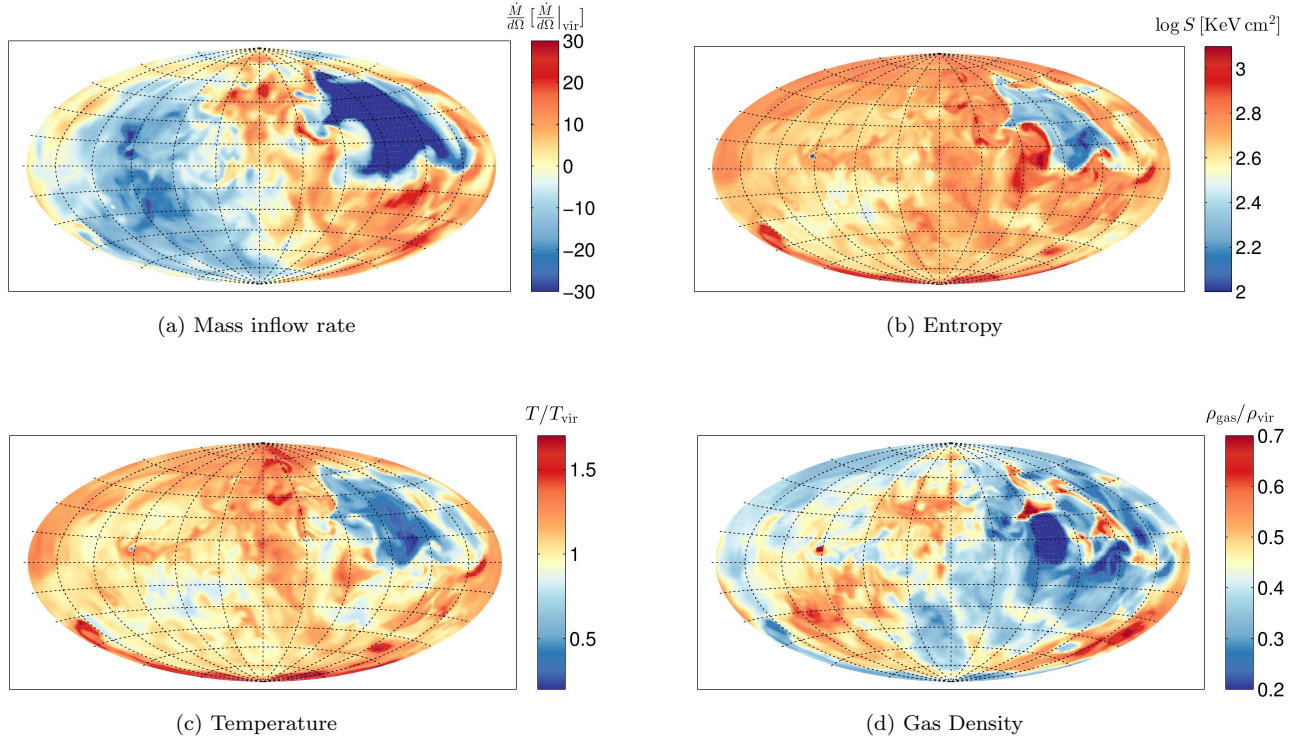


Figure 10. Hammer projections of a thin spherical shell of radius $0.3R_{\text{vir}}$ of the cluster CL6 shown in Fig. 4. Plotted are the mass inflow rate (a), entropy (b), temperature (c) and density (d). A prominent inflowing streams is clearly seen in the top-right quadrant, characterized by strong inflow and lower temperature and entropy than its surroundings.

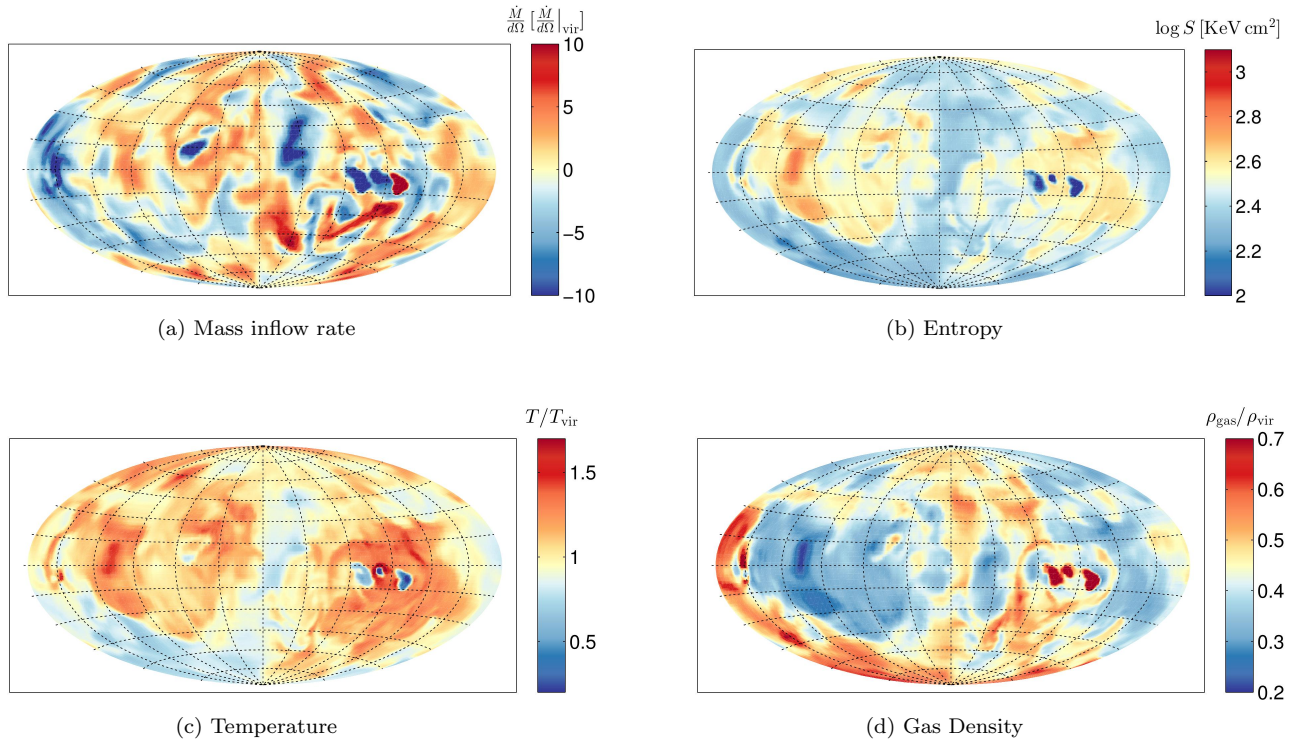


Figure 11. Hammer projections of a thin spherical shell of radius $0.3R_{\text{vir}}$ of the cluster CL14 shown in Fig. 7. Plotted are the mass inflow rate (a), entropy (b), temperature (c) and density (d). Mass inflow and outflow occur on small areas. Several small high-density cool clumps can be seen on the 'equator' in the right half of the plots.

in stream penetration in the cluster is accompanied by a change in relaxedness, changing from NR at $z = 0.6$ to R at $z = 0$ (see Tables 1 and 2).

The penetration of streams can also grow over time as can be seen in Figs. 9a and 9b where we show the cluster CL11 at $z = 0.6$ and $z = 0$, respectively. At $z = 0.6$, the maximal penetration is found in a stream entering from the top, which penetrates to just outside the $0.25R_{\text{vir}}$ mark. At $z = 0$, the streams can be seen to penetrate deep into the very centre of the cluster.

In order to study the individual stream penetration properties of each cluster in detail, we employed a two-pronged approach. A simple stream-identification algorithm to identify the maximal penetration point of the streams in each cluster was constructed and in addition, visual identification of the streams was carried out in two complementary methods. The results of quantitative and visual methods were compared and combined yielding a robust estimate of the maximal penetration of the streams in all the clusters.

The stream identification algorithm was based on the high mass inflow rates and entropy properties of the streams and on the fact that the streams are supersonic with respect to their surroundings (see e.g., Figs. 4, 5 and 10). To ensure that large-scale streaming features are identified, rather than isolated clumps and satellites, the simulation data was spatially smoothed over a scale of 100 kpc comoving (62.5 kpc proper at $z = 0.6$).

In the smoothed data, streams were defined by including simulation cells which simultaneously met the following four conditions:

- The mass inflow rate in the cell is at least three times the virial accretion rate of eq. (13). This of course entails that the radial velocity in the cell is negative.
- The entropy in the cell is lower than the average entropy of all the cells found at the same radial distance.
- A ratio of 0.9 or higher between the gas velocity in the cell and the typical speed of sound at the cell radius as defined in eq. (14).
- No stellar particles are found in the cell, thus ensuring that satellite galaxies are removed.

Once all the cells comprising the streams in a given cluster were identified, the maximal penetration depth can be easily found.

To complement the stream identification algorithm, we carried out a visual determination of the maximal penetration depth of the streams. This was done by examining the clusters as a series of spherical shells by use of Hammer projections³ and by standard Cartesian projections.

We follow the streams in each cluster as they flow into the cluster from outside the virial radius until they can no longer be distinguished from their surroundings. This was done by inspecting Hammer projections of spherical shells at different radii of the temperature, density, mass inflow rate and entropy for all the clusters (examples are shown for CL6 and CL14 at $0.3R_{\text{vir}}$ in Figs. 10 and 11).

Gas streams are identified in a Hammer projection of a given radial shell as areas of which meet the same set of

criteria used in the stream identification algorithm, namely areas of enhanced inflow, at least three times the virial accretion rate of eq. (13), in which the entropy is lower than the mean entropy of the shell. In addition, the stream signature must be continuous over several spherical shells (~ 300 kpc), so as not to include isolated clumps.

Only streams which originate beyond the virial radius at $\gtrsim 4$ Mpc and persist to within R_{vir} are considered. The Hammer projections for a shell at $0.3R_{\text{vir}}$ for a cluster in which the streams penetrate to the centre (CL6) and for a cluster in which the streams are stopped at $r \approx 0.5R_{\text{vir}}$ (CL14) are shown in Figs. 10 and 11, respectively.

The prominent stream found in CL6 (Figs. 4 and 5) is clearly seen in the upper-right quadrant of the Hammer plots, characterized by its high inflow, cooler temperature and elevated density. No such stream is seen in CL14, but several small clumps can be seen on the ‘equator’ of the projections on the right half, characterized by high density and low temperatures.

It is instructive to compare the mass inflow rate maps between the two clusters, Figs. 10a and 11a, taking note of the different colour scale of the two plots which highlight the large difference in the mass accretion rate of the two clusters. In CL6, the large stream covers a large area in the plot, whereas in CL14 inflowing and outflowing areas subtend a much smaller solid angle and are also of markedly lower magnitude.

To complement the visual stream penetration analysis, we examined mass inflow maps of all the clusters in all three Cartesian projections (e.g. Figs. 5 and 7 to 9). Once again, gas streams were identified visually based on the same criteria as before. By visually examining the clusters both from the point of view of an outside observer (Cartesian projection maps) and from the point of view of an observer at the centre of the cluster (Hammer projections), we achieve a much more comprehensive estimate of the penetration depth of the streams.

The error in ascertaining the maximal penetration depth of the streams is based on the smoothing scale used in the stream identification algorithm, and the cell size of the simulation (~ 5 kpc comoving), which also sets the radial spacing of the spherical shells. In the Cartesian projections, the error is of order several times the cell size. In the Hammer projections, the shell thickness is twice the cell size and once again the error is of order several times the shell thickness. As a result, we estimate that the error in determining the maximal penetration to be no more than ± 50 kpc comoving.

It stands to reason that in a cluster with deeply penetrating streams, the high mass and energy inflow rate into the central regions will have an important effect on the properties of the ICM. The energy associated with a strong inflow of matter can heat its surroundings, drive random motions and thus create a system which is dynamically NR.

Our findings concerning the correlation between stream penetration and relaxedness are summarized in Fig. 12, which shows the maximal stream penetration into the clusters in the simulations suite at $z = 0$ and at $z = 0.6$. Each cluster is represented by a coloured circle on the plane, with a label identifying the cluster, such that its X coordinate shows the maximal penetration into the cluster at $z = 0$ and its Y coordinate shows the penetration at $z = 0.6$. The uncertainty in the determination of the penetration depth is

³ Hammer projections are equal-area projections of a spherical surface to a 2D map.

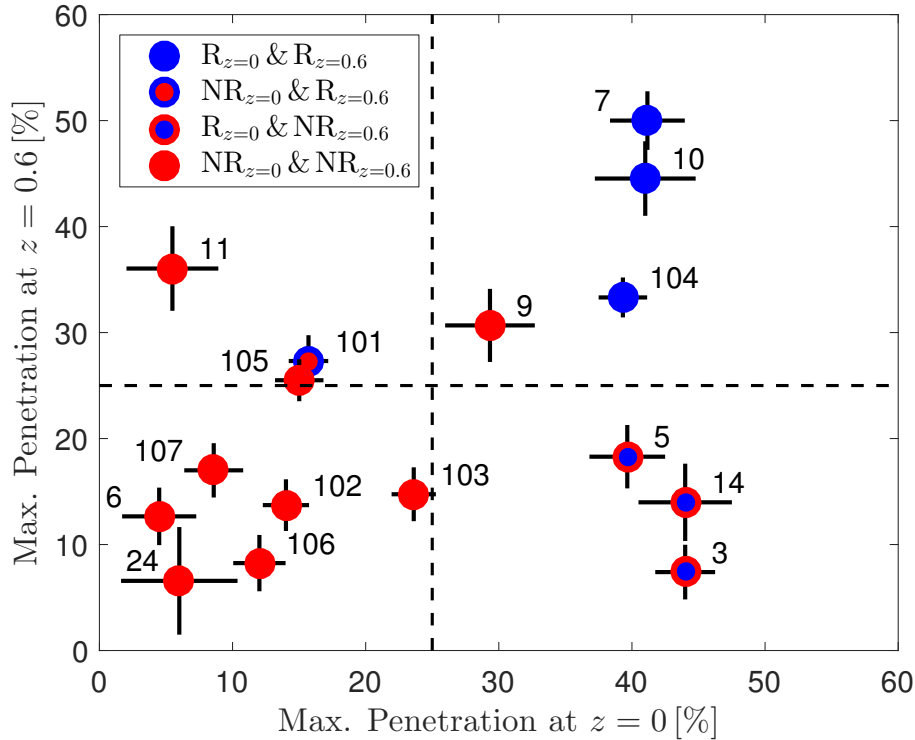


Figure 12. The link between the relaxedness and the maximal penetration of streams in the simulated cluster suite. The axes show the maximal penetration of streams into the clusters at $z = 0$ and $z = 0.6$ (X and Y axes respectively), in per cent of the virial radius R_{vir} . The colours mark the dynamical state of the clusters. Clusters which are R at both epochs are marked in blue, while clusters which are NR at those times are marked in red. Clusters which were NR at $z = 0.6$ but are R at $z = 0$ are shown as blue circles with red outlines, while clusters which were R at $z = 0.6$ but are NR at $z = 0$ are shown as red circles with blue outlines. The uncertainties in determining the penetration depth are shown by the black horizontal and vertical lines. The black dashed lines mark the $0.25R_{\text{vir}}$ region. The link between stream penetration and relaxedness is evident – deeply penetrating streams are found only in NR clusters and all but two of the NR clusters host deeply penetrating streams. Of particular interest are the three clusters found in the bottom-right quadrant, which host deeply penetrating streams at $z = 0.6$ but not at $z = 0$, and whose dynamical classification changes from NR to R accordingly. CL101 found in the top-left quadrant, also changed from R at $z = 0$ to NR at $z = 0.6$ in conjunction with an increase in stream penetration between the two epochs.

marked by the black lines. The units of penetration are in per cent of R_{vir} for each cluster, thus the streams in cluster CL3 penetrate to ~ 5 per cent of R_{vir} at $z = 0.6$ (Fig. 8a) but at $z = 0$ penetrate only to ~ 36 per cent of R_{vir} (Fig. 8b).

The colours of the circles indicate the dynamical state of the cluster (R versus NR) at the two epochs: clusters which are R at both epochs are represented by blue circles and clusters which are NR at both epochs are marked as red circles. Clusters which are NR at $z = 0.6$ but R at $z = 0$ are marked as blue circles with red outlines and clusters which are R at $z = 0.6$ and NR at $z = 0$ are shown as red circles with blue outlines.

It is immediately apparent that there exists a correlation between penetration and relaxedness. Of the 10 NR clusters at $z = 0$ all but one are characterized by streams which penetrate to within $0.25R_{\text{vir}}$ and four of them host streams which penetrate to within $0.1R_{\text{vir}}$. Meanwhile, none of the six R clusters at $z = 0$ host a stream which penetrates deeper than $0.4R_{\text{vir}}$. By and large this relationship holds at $z = 0.6$. Of the four R clusters at that epoch none have streams which penetrate into the inner regions. Most of the NR clusters, 10 out of 12, host streams which penetrate to at least $0.25R_{\text{vir}}$ and half of those penetrate to within $0.15R_{\text{vir}}$.

Especially interesting are the clusters CL3, CL5 and CL14 (found in the bottom-right quadrant of Fig. 12), which are characterized by deeply penetrating streams at $z = 0.6$ which no longer penetrate into the central regions at $z = 0$. For these clusters, the transition between penetrating to non-penetrating streams is accompanied with a change of classification from NR to R, strengthening the relation between stream penetration and unrelaxedness. In the cluster CL101 the opposite trend is observed, with the cluster transitioning from R at $z = 0.6$ to NR at $z = 0$ with a corresponding increase in stream penetration between the two epochs.

At $z = 0.6$, two exceptions are found, CL9 and CL11, which are classified as NR but do not exhibit strongly penetrating streams. A possible explanation for these clusters, besides the possibility that they are mis-classified as NR, is that a process other than smooth stream penetration is responsible for the NR status of the cluster, such as an ongoing merger event. Examination of these systems reveals that at $z = 0.6$ both CL11 and CL9 host multiple X-ray peaks in their centres which can account for the NR classification. In the next section, we address the role of gas streams versus satellite haloes in determining the dynamical state of the clusters.

The cluster CL9 is classified as NR at $z = 0$, but hosts streams which only penetrated to within $0.29R_{\text{vir}}$. Since this is the only case in which the penetration is somewhat at odds with the relaxedness we consider it to be an isolated anomaly.

5 GAS STREAMS VERSUS MERGERS

In the previous section, we found a strong correlation between the penetration of gas streams into the cluster and the dynamical state of the system, which suggests that the strong inflows of mass into the central regions of clusters drive random gas motions and lead to dynamically unrelaxed systems. A question naturally arises regarding the importance of gas streams in determining the classification into R and NR, compared to other factors such as satellites and mergers, which are known causes for NR clusters (Burns et al. 2008). Since the gas streams originate in the large-scale filaments of the cosmic web, and indicate the preferred directions along which mass accretion takes place, it is reasonable to assume that satellites will be found preferentially along the streams, especially on their way in for the first time. This begs the question: could both the relaxedness and stream penetration properties be correlated with the presence of satellites or other substructures in the cluster without being linked directly?

As described in §2, the hallmarks of an NR cluster are the existence of secondary luminosity peaks in the X-ray emission, significant shifts of the centres of the isophotes and filamentary X-ray structures. R clusters, on the other hand, are characterized by isophotes with only small deviations from elliptical symmetry. The mere existence of some substructure within the cluster is of course not necessarily a sign of unrelaxedness, otherwise all clusters would be classified as NR, seeing as all clusters contain substructures to a certain degree. Identification of these features in mock X-ray images, which may suffer from projection effects, and is carried out subjectively, as is also the case in observations.

The existence of a secondary luminosity peak in the central regions is a clear mark of a merger event (except in the case of projection effects). X-ray filamentary structure can occur either as a result of stripped gas forming an extended emission area behind (or ahead) of the sub-clump/galaxy or as a result of several separate substructures forming an apparent filament due to projection effects. In our analysis, we found that the large-scale gas streams themselves do not register as filamentary X-ray structures. Isophotal centroid shifts and deviations from elliptical symmetry may be the result of substructure, but as we shall see, can also occur due to the inflowing streams.

We explore the relation between the smooth streams and the observational signatures of relaxedness by examining maps of the mass inflow rate in the clusters overlaid with X-ray isophotes. We examine the cluster on the scale of $R_{500,c}$, that is the radius at which the mean density is 500 the critical density of the universe. $R_{500,c} \simeq 0.45R_{\text{vir}}$ based on eq. (2). Several representative examples of NR clusters are shown in Fig. 13, and an example of an R cluster is shown in Fig. 14.

It is important to stress that the images shown here were *not* used to determine the dynamical classification. As

noted earlier, the dynamical classification to R and NR was based on mock *Chandra* observation of the clusters which took into account instrument sensitivity, exposure times and other observational considerations Nagai et al. (2007a,b), which we do not address here.

The X-ray emission per unit volume from a gas element is calculated by

$$L_X = \left(\frac{\chi}{\mu m_p} \right)^2 \rho_g^2 \Lambda(T, Z). \quad (39)$$

The X-ray isophotes are determined by summing the X-ray luminosity along the line of sight for a given projection.

In Fig. 13a, the inflowing smooth stream from the bottom, overshoots the centre and shocks against gas coming in from the top (Fig. 6). The isophotes in the centre are distorted in the region of the inflowing stream and the plume shaped outflow, which results in an NR classification, despite the relative dearth of significant substructure in the cluster, seen as small blobs in the isophotes. The distortions in the isophotes also do not correlate with the positions of the substructures seen in the cluster. A similar effect can be seen in Fig. 13d where the isophotes are distorted due to the incoming smooth stream on the bottom left leading to a significant deviation from elliptical symmetry. Here too the small amount and size of the substructure, as well as their positions, cannot account for the distortions in the isophotes which attest to the unrelaxedness of the cluster. In Fig. 13c, the isophotes are also skewed due to the incoming smooth stream with small signatures of substructures found in the cluster.

In Fig. 13b, two luminosity peaks can be found in the central region, one at a position of (0,0) and the other at a position of roughly $(-0.1, 0)$, indicating a merger in the system. The cluster is classified as NR, due to the combined effect of the merger and the deeply penetrating stream it hosts. Examining the isophotes beyond the merger event, we find that they trace the shock fronts which formed at the collision sites between the inflowing smooth streams coming from the top and the bottom of the plot. The density and temperature jump associated with the shock lead to an enhancement of the X-ray luminosity accounting for this feature (this can also be seen in Figs. 13a and 13c). Thus, even if the cluster was not in the throes of a merger event, the distorted isophotes which trace the shock fronts would still lead to an NR classification.

The combined sample of clusters at both redshifts contains 22 NR clusters: 10 at $z = 0$ and 12 at $z = 0.6$. Of these, only in nine clusters can the dynamical state be unequivocally linked to mergers and substructures, by dint of the existence of secondary luminosity peaks or filamentary structure (e.g. Fig. 13b). In nine additional clusters, the contribution of substructure to the non-relaxedness is seen to be of minor importance in light of the small number and size of the observed substructure, and the unrelaxedness is due primarily to the smooth streams (e.g. Figs. 13a, 13c and 13d). In the remaining four systems it is unclear what is the relative contribution of the streams and substructure to the NR state of the cluster. In all likelihood, it is the combined effect of the streams and the substructures which lead to the unrelaxedness.

In light of these findings, we conclude that there is a real connection between smooth stream penetration and the

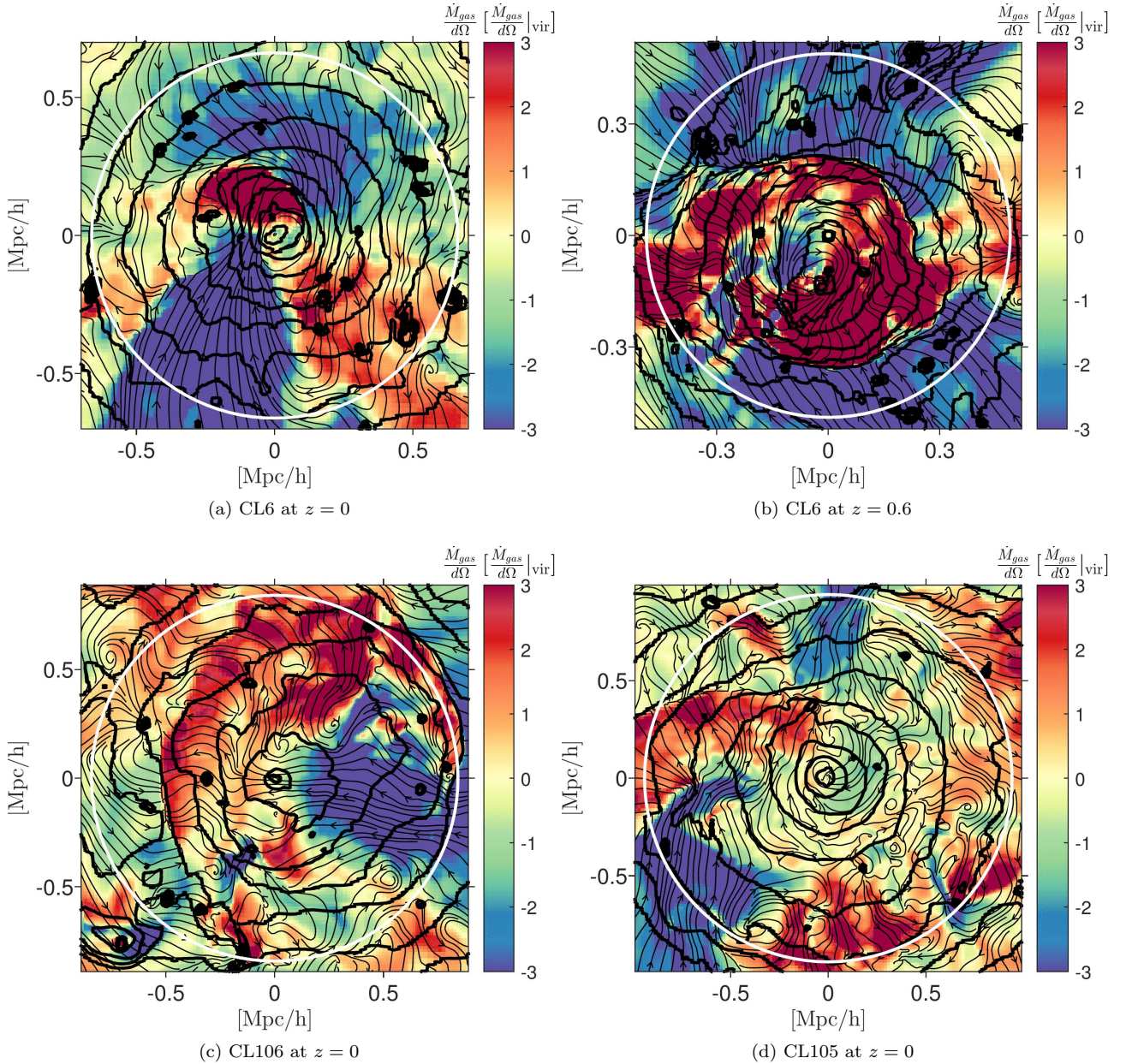


Figure 13. The relation between gas streams and relaxedness is explored in colour maps of the mass inflow rate overlaid with X-ray isophotes (black contours), on the scale of $R_{500,c}$ (white circle). The velocity field is shown with black streamlines. Four representative NR clusters are shown: CL6 at $z = 0$ and $z = 0.6$ (a) & (b), CL106 at $z = 0$ (c) and CL105 at $z = 0$ (d).

relaxedness of the systems. The correlation found in Fig. 12 is not an artefact of the correlation between the streams and substructures and the unrelaxedness of a cluster is not caused solely by mergers.

6 DISCUSSION

Galaxy clusters are classified as R or NR based on observational signatures of dynamical activity. We utilized a suite of simulated cluster systems, each classified as R or NR based on the same observational parameters employed for observed clusters, to study the source of this classification.

Our starting point in the analysis was to relate the clas-

sification, based on mock observations, to the actual dynamical forces at play in the system. We employed a form of the Jeans equation for the radial velocity component, modified for the Eulerian simulation scheme, which resulted in an equation of motion for spherical gas shells. In the NR clusters, we find that a higher fraction of the pressure support against gravity originates in non-thermal processes, mostly due to random gas motions. As a result, these clusters are not in steady-state equilibrium. In R clusters, the non-thermal contributions are lower by a factor ~ 2 compared to the NR clusters, except within the very centre of the system ($r \lesssim 0.05 R_{vir}$).

The increased level of gas motions in the NR cluster

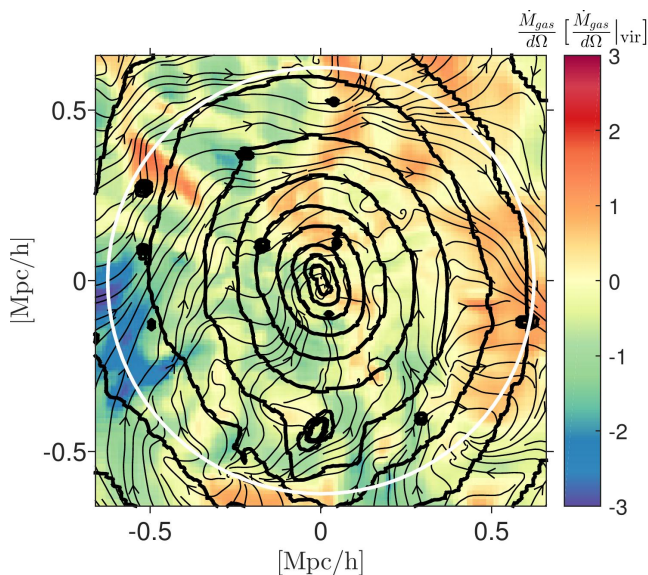


Figure 14. An example of a R cluster, CL7 at $z = 0$. Colour maps of the mass inflow rate overlaid with X-ray isophotes (black contours), on the scale of $R_{500,c}$ (white circle). The velocity field is shown with black streamlines. Substructure within $R_{500,c}$ does not preclude a dynamically relaxed state.

population is matched by higher mass inflow rates in these clusters, compared to the R cluster population. The picture that emerges is that the higher inflow rates bring in more energy and momentum, which allow deeper penetration of the streams which can then drive random motions in the cluster, stirring it up and leading to a dynamically disturbed system.

The significant role the build-up of turbulence plays in determining the properties of the ICM has been well established (Parrish et al. 2010; Hallman & Jeltema 2011; Nelson et al. 2012; Lau et al. 2013; Nelson et al. 2014a). Other studies have also shown that the turbulent pressure created by the random motions of the gas is important in stabilizing the system and in the central regions may be the dominant force fighting the pull of gravity (Lau et al. 2009; Nelson et al. 2014b). Zhuravleva et al. (2014) have shown that the heating rate due to the dissipation of turbulence may be sufficient to offset the radiative cooling in the cluster centres. The random motions can also lead to the dispersal of metals over larger volumes in the central regions, as is seen in observations (De Grandi & Molendi 2002; Rebusco et al. 2005, 2006; Simionescu et al. 2015).

While treating the clusters as spherical systems can yield important insights, a full understanding of the structure and dynamics of the ICM can only be achieved by studying the full 3D structure of the system. The main reason for this is the asymmetric nature of gas accretion into the cluster which occurs along large-scale gas streams which originate from the cosmic web. These streams play an important role in determining the behaviour of the system, especially in the central regions.

The gas streams are a prominent feature in the clusters, especially in terms of entropy and inflow rate. Mass inflow rate into the system occurs almost solely along the gas streams. The gas within the stream has undergone early

shock heating when it was accreted to the stream long before entering the cluster and is heated further via weak shocks within the stream. As a result, the stream temperatures are $\gtrsim 10^6$ K before entering the cluster, earning them the name ‘warm streams’. After crossing the virial radius the streams are heated to $\sim T_{\text{vir}}$, and are not significantly cooler than their surroundings.

The inflowing streams carry a significant amount of energy with them, not much lower than the entire radiative output of the cluster, only a fraction of which is lost to radiation as they flow towards the centre. The energy is deposited in the region where the stream disrupts and dissipates. In our study, we find some gas streams which penetrate into the centre of the clusters while others were stopped at larger radii. Examining the clusters at two epochs, $z = 0$ and $z = 0.6$, reveals that the penetration depth of streams may evolve over time. In some cases, streams which penetrated into the centre in early times have been ‘pushed out’ and dissipate at larger radii at $z = 0$, while in other cases the opposite occurs with streams which increase their penetration depth over time. The cause of the possible disruption of streams at a given radius is an interesting open issue, one which we plan to address in future studies (Mandelker et al., in preparation; Padnos et al., in preparation).

A deeply penetrating stream, depositing its energy in the very centre of the cluster, may have a profound effect on the dynamics of the ICM in that region. Examining our simulated clusters, we find a strong connection between the dynamic state of a cluster and the presence of a deeply penetrating stream. All but two of the 22 NR clusters, comprised of clusters at both epochs, possess at least one stream which penetrates to $r \lesssim 0.25R_{\text{vir}}$ whereas the penetration into R clusters does not exceed $0.35R_{\text{vir}}$, with one exception.

Especially interesting are three clusters which possessed deeply penetrating streams at $z = 0.6$ but by $z = 0$ no streams were found in their central regions. In conjunction, the dynamic classification of these clusters changed from NR to R. In another cluster, the penetration of the streams increased between the two epochs and the cluster transitioned from R to NR accordingly. This strengthens the link established between the two properties.

An important result of this paper is that the build-up of random motions can occur not only due to episodic merger events (Vazza et al. 2011; Nelson et al. 2012), but also by the continuously inflowing gas streams originating from the large-scale filamentary structure of the cosmic web. We have taken special care to ensure that there is indeed a direct link between deeply penetrating gas streams and the NR dynamical classification in the relevant clusters, besides the effect of merging substructure, which is known to induce dynamical disturbance in the ICM.

Clusters which are R are often also CC clusters (Sander et al. 2009a; Walker et al. 2012) whereas the NCC clusters are often associated with NR clusters. The common wisdom is that a CC cannot easily form in a dynamically disturbed environment. In this manner, it may be that the dichotomous population of CC versus NCC clusters is a direct and natural result of stream penetration in clusters. This scenario complements the work of Burns et al. (2008) in the sense that the key factor in preventing the formation of CC is a strong mass (and energy) inflow into the core of the system, whether it be in the form of smooth streams

or mergers. [Birnbom & Dekel \(2011\)](#) have also shown that infalling gas clumps can be an effective form of heating the ICM.

We note that our simulation suite, which reproduces the R–NR dichotomous population, does not explicitly reproduce the associated CC–NCC dichotomy population. Rather, all the clusters, both R and NR, suffer from central overcooling and thus possess a density peak reminiscent of a CC cluster, over a region which is only barely resolved by the simulation mesh. It is likely that this is due to the numerical limitations of the simulation but it is also possible that key physical process is missing, such as AGN feedback and thermal conduction.

If the latter is the case, we find that the energy injected by the streams is not sufficient on its own to offset the runaway cooling in CC clusters. However, the random gas motions stirred by the streams may increase the effectiveness of the AGN heating. Examination of new simulations with higher resolution will be able to shed light on whether the gas streams on their own can avert the overcooling or whether they are only one of a number of players which lead to the formation of NCC clusters.

Since the streams are the principal channels of mass accretion into the clusters, sub-haloes, gas clumps and satellites are also expected to be found along the streams. This makes it difficult to disentangle the contribution of the smooth versus clumpy accretion to the heating and build-up of random gas motions in the central regions of the ICM. One may argue that for some purposes such a distinction is superfluous and that accretion is accretion, regardless of its form.

However, since the relevant physical processes, such as ram-pressure stripping, hydrodynamical drag, tidal stripping etc., act differently on clumps and streams, it may be necessary in some cases to differentiate between the different forms of accretion. Tidal interactions are sensitive to the geometrical shape of the interacting bodies and thus the forces acting on a clump and stream in the tidal field of the host cluster will be very different. Dynamical friction is another physical process which may affect clumps and streams in a different manner.

Another key difference is that clumps of gas, if they are not disrupted, may travel through the centre of the cluster and affect the ICM for much longer periods ([Birnbom & Dekel 2011](#)) and over larger areas than streams which are dispersed once they reach the centre.

As we have seen, the penetration depth of a stream can change in a given cluster over time and so does the dynamical state of the cluster. Thus, a cluster may evolve from being an NR cluster to a R cluster, and vice-versa. In our simulation suite, we have found three examples of NR to R transitions, and one of R to NR all of which are linked to changes in the stream penetration depth. [Rossetti & Molendi \(2010\)](#) found that most observed NCC clusters in their observed sample host regions which have some characteristics of CC, such as low-entropy gas and high metal abundances, supporting the notion that clusters alternate between the CC and NCC state.

In our scenario, transition from an NR to R cluster involves the dissipation of the random gas motions in the central regions which we estimate to take of the order of several giga years. This is in agreement with [Hallman & Jeltama](#)

(2011) who find the turbulence dissipation time-scale to be ~ 1 Gyr. [Rossetti et al. \(2011\)](#) estimate that in observed clusters, the typical transition time-scale in which an NCC relaxes into a CC is ~ 3 Gyr.

An interesting issue worthy of follow-up research is the interplay between the effects of gas streams and AGN on the ICM. Turbulent motions have been suggested as a mechanism for spreading the energy supplied by an AGN through jets over large volumes ([McNamara & Nulsen 2007](#)). If the central regions of the cluster have already been stirred up by the infalling gas streams, the effectiveness of the AGN in heating the ICM may be bolstered. A study of this issue would require simulations which incorporate both AGN models and sufficient resolution to model the gas motions generated by the streams in the central regions.

The analysis of the effects of streams on the structure of cluster, particularly in relation to the formation of CC versus NCC systems, would be incomplete without a detailed examination of the heating and cooling processes in the inner regions. This will allow one to assess whether the energy brought in by the streams is effective in heating the central regions or not.

7 SUMMARY

In this paper, we have revealed the existence of large-scale gas streams in clusters and explored how they affect their host systems, specifically in relation to the dynamical state of the cluster. We summarize our main conclusions below.

- NR clusters are characterized by higher levels of non-thermal pressure support against gravity, mostly due to random gas motion, compared to R clusters. This is due to the higher mass inflow rates found in these clusters.
- The mass inflow occurs predominantly along gas streams which originate in the cosmic web and flow into the cluster. These streams are not significantly cooler than the surrounding ICM ('warm streams'). Some streams are found to penetrate into the very centre of the cluster, while others are stopped abruptly before reaching the centre.
- A strong connection was established between the dynamical state of the cluster (R versus NR) and the presence of at least one deeply penetrating stream. The degree of penetration was found to change over time coupled with a corresponding change in dynamical state. In this manner, the observed R versus NR dichotomous population, was found to be a natural result of the degree of stream penetration into the cluster.
- The deeply penetrating streams can carry large amounts of energy and momentum into the very centre of the cluster. These can drive the random gas motions in the cluster centre which account for the NR state of the cluster.

The study of these objects is still in its early stages and we are confident that with better simulations and more advanced observational instruments, much more can be learned about the gas streams which may help answer some of the important open questions which pertain to the understanding the structure and evolution of galaxy clusters.

ACKNOWLEDGMENTS

We acknowledge stimulating discussions with Nir Shaviv and Alexey Vikhlinin. This work was partly supported by the grants ISF 124/12, I-CORE Program of the PBC/ISF 1829/12, BSF 2014-273, and NSF AST-1405962.

REFERENCES

- Ascasibar Y., Markevitch M., 2006, *ApJ*, 650, 102
 Birnboim Y., Dekel A., 2003, *MNRAS*, 345, 349
 Birnboim Y., Dekel A., 2011, *MNRAS*, 415, 2566
 Birnboim Y., Dekel A., Neistein E., 2007, *MNRAS*, 380, 339
 Bonafede A., Vazza F., Brüggén M., Murgia M., Govoni F., Feretti L., Giovannini G., Ogrean G., 2013, *MNRAS*, 433, 3208
 Brown S., Rudnick L., 2011, *MNRAS*, 412, 2
 Bryan G. L., Norman M. L., 1998, *ApJ*, 495, 80
 Bullock J. S., Kolatt T. S., Sigad Y., Somerville R. S., Kravtsov A. V., Klypin A. A., Primack J. R., Dekel A., 2001, *MNRAS*, 321, 559
 Buote D. A., Tsai J. C., 1996, *ApJ*, 458, 27
 Burns J. O., 1998, *Science*, 280, 400
 Burns J. O., Hallman E. J., Gantner B., Motl P. M., Norman M. L., 2008, *ApJ*, 675, 1125
 Chen Y., Reiprich T. H., Böhringer H., Ikebe Y., Zhang Y.-Y., 2007, *A&A*, 466, 805
 Churazov E., Forman W., Jones C., Böhringer H., 2003, *ApJ*, 590, 225
 Churazov E., Forman W., Vikhlinin A., Tremaine S., Gerhard O., Jones C., 2008, *MNRAS*, 388, 1062
 Danovich M., Dekel A., Hahn O., Teyssier R., 2012, *MNRAS*, 422, 1732
 De Grandi S., Molendi S., 2002, *ApJ*, 567, 163
 De Grandi S., Ettori S., Longhetti M., Molendi S., 2004, *A&A*, 419, 7
 Dekel A., Birnboim Y., 2006, *MNRAS*, 368, 2
 Dekel A., Birnboim Y., 2008, *MNRAS*, 383, 119
 Dekel A., et al., 2009, *Nature*, 457, 451
 Dekel A., Zolotov A., Tweed D., Cacciato M., Ceverino D., Primack J. R., 2013, *MNRAS*, 435, 999
 Diemer B., Kravtsov A. V., 2014, *ApJ*, 789, 1
 Dietrich J. P., Werner N., Clowe D., Finoguenov A., Kitching T., Miller L., Simionescu A., 2012, *Nature*, 487, 202
 Eckert D., et al., 2015, *Nature*, 528, 105
 Ferland G. J., Korista K. T., Verner D. A., Ferguson J. W., Kingdon J. B., Verner E. M., 1998, *PASP*, 110, 761
 Finoguenov A., Briel U. G., Henry J. P., 2003, *A&A*, 410, 777
 Gheller C., Vazza F., Favre J., Brüggén M., 2015, *MNRAS*, 453, 1164
 Haardt F., Madau P., 1996, *ApJ*, 461, 20
 Hahn O., Martizzi D., Wu H.-Y., Evrard A. E., Teyssier R., Wechsler R. H., 2015, preprint
 Hallman E. J., Jeltema T. E., 2011, *MNRAS*, 418, 2467
 Iapichino L., Brüggén M., 2012, *MNRAS*, 423, 2781
 Kennicutt Jr. R. C., 1998, *ApJ*, 498, 541
 Kereš D., Katz N., Weinberg D. H., Davé R., 2005, *MNRAS*, 363, 2
 Kereš D., Katz N., Fardal M., Davé R., Weinberg D. H., 2009, *MNRAS*, 395, 160
 Klar J. S., Mücke J. P., 2012, *MNRAS*, 423, 304
 Klypin A., Kravtsov A. V., Bullock J. S., Primack J. R., 2001, *ApJ*, 554, 903
 Kravtsov A. V., 1999, Ph.d. thesis, NEW MEXICO STATE UNIVERSITY, <http://adsabs.harvard.edu/abs/1999PhDT.....25K>
 Kravtsov A. V., Vikhlinin A., Nagai D., 2006, *ApJ*, 650, 128
 Lau E. T., Kravtsov A. V., Nagai D., 2009, *ApJ*, 705, 1129
 Lau E. T., Nagai D., Kravtsov A. V., Zentner A. R., 2011, *ApJ*, 734, 93
 Lau E. T., Nagai D., Nelson K., 2013, *ApJ*, 777, 151
 Lau E. T., Nagai D., Avestruz C., Nelson K., Vikhlinin A., 2015, *ApJ*, 806, 68
 Mac Low M.-M., Klessen R. S., Burkert A., Smith M. D., 1998, *Physical Review Letters*, 80, 2754
 Markevitch M., Vikhlinin A., 2007, *Phys. Rep.*, 443, 1
 Markevitch M., et al., 2000, *ApJ*, 541, 542
 McNamara B. R., Nulsen P. E. J., 2007, *ARA&A*, 45, 117
 Molnar S. M., Hearn N., Haiman Z., Bryan G., Evrard A. E., Lake G., 2009, *ApJ*, 696, 1640
 Molnar S. M., Chiu I.-N., Umetsu K., Chen P., Hearn N., Broadhurst T., Bryan G., Shang C., 2010, *ApJ*, 724, L1
 More S., Diemer B., Kravtsov A. V., 2015, *ApJ*, 810, 36
 Mushotzky R. F., Loewenstein M., 1997, *ApJ*, 481, L63
 Nagai D., Kravtsov A. V., 2003, *ApJ*, 587, 514
 Nagai D., Vikhlinin A., Kravtsov A. V., 2007a, *ApJ*, 655, 98
 Nagai D., Kravtsov A. V., Vikhlinin A., 2007b, *ApJ*, 668, 1
 Navarro J. F., Frenk C. S., White S. D. M., 1996, *ApJ*, 462, 563
 Navarro J. F., Frenk C. S., White S. D. M., 1997, *ApJ*, 490, 493
 Neistein E., Dekel A., 2008, *MNRAS*, 383, 615
 Nelson K., Rudd D. H., Shaw L., Nagai D., 2012, *ApJ*, 751, 121
 Nelson K., Lau E. T., Nagai D., Rudd D. H., Yu L., 2014a, *ApJ*, 782, 107
 Nelson K., Lau E. T., Nagai D., 2014b, *ApJ*, 792, 25
 Ocvirk P., Pichon C., Teyssier R., 2008, *MNRAS*, 390, 1326
 Parrish I. J., Quataert E., Sharma P., 2010, *ApJ*, 712, L194
 Peterson J. R., Fabian A. C., 2006, *Phys. Rep.*, 427, 1
 Pinto C., et al., 2015, *A&A*, 575, A38
 Rasia E., Tormen G., Moscardini L., 2004, *MNRAS*, 351, 237
 Rasia E., et al., 2015, *ApJ*, 813, L17
 Rebusco P., Churazov E., Böhringer H., Forman W., 2005, *MNRAS*, 359, 1041
 Rebusco P., Churazov E., Böhringer H., Forman W., 2006, *MNRAS*, 372, 1840
 Roediger E., Brüggén M., Simionescu A., Böhringer H., Churazov E., Forman W. R., 2011, *MNRAS*, 413, 2057
 Rossetti M., Molendi S., 2010, *A&A*, 510, A83
 Rossetti M., Eckert D., Cavalleri B. M., Molendi S., Gastaldello F., Ghizzardi S., 2011, *A&A*, 532, A123
 Sanders J. S., Fabian A. C., Smith R. K., 2011, *MNRAS*, 410, 1797
 Sanderson A. J. R., Ponman T. J., O'Sullivan E., 2006, *MNRAS*, 372, 1496
 Sanderson A. J. R., O'Sullivan E., Ponman T. J., 2009a, *MNRAS*, 395, 764
 Sanderson A. J. R., Edge A. C., Smith G. P., 2009b, *MNRAS*, 398, 1698
 Sarazin C. L., 1988, X-ray emission from clusters of galaxies. Cambridge Astrophysics Series, Cambridge: Cambridge University Press, 1988, <http://adsabs.harvard.edu/abs/1988xrec.book.....S>
 Simionescu A., et al., 2013, *ApJ*, 775, 4
 Simionescu A., Werner N., Urban O., Allen S. W., Ichinohe Y., Zhuravleva I., 2015, *ApJ*, 811, L25
 Smith G. P., Kneib J.-P., Smail I., Mazzotta P., Ebeling H., Czoske O., 2005, *MNRAS*, 359, 417
 Sutherland R. S., Dopita M. A., 1993, *ApJS*, 88, 253
 Suto D., Kawahara H., Kitayama T., Sasaki S., Suto Y., Cen R., 2013, *ApJ*, 767, 79
 Tozzi P., Rosati P., Ettori S., Borgani S., Mainieri V., Norman C., 2003, *ApJ*, 593, 705
 Vazza F., Brunetti G., Gheller C., Brunino R., Brüggén M., 2011, *A&A*, 529, A17
 Vazza F., Eckert D., Simionescu A., Brüggén M., Ettori S., 2013, *MNRAS*, 429, 799

- Walker S. A., Fabian A. C., Sanders J. S., George M. R., 2012, [MNRAS](#), 427, L45
- Wechsler R. H., Bullock J. S., Primack J. R., Kravtsov A. V., Dekel A., 2002, [ApJ](#), 568, 52
- Werner N., Finoguenov A., Kaastra J. S., Simionescu A., Dietrich J. P., Vink J., Böhringer H., 2008, [A&A](#), 482, L29
- Zhuravleva I., et al., 2014, [Nature](#), 515, 85

This paper has been typeset from a \TeX / \LaTeX file prepared by the author.